Cambridge Centre for Computational Chemical Engineering

University of Cambridge

Department of Chemical Engineering

Preprint ISSN 1473 – 4273

A statistical approach to develop a detailed soot growth model using PAH characteristics

Abhijeet Raj [1] , Matthew S Celnik [1] , Raphael Shirley [1] ,

Markus Sander [1] , Robert Patterson [1] , Richard H West [1] , Markus Kraft [1] *

released: 04 July 2008

[1] Department of Chemical Engineering
University of Cambridge
New Museums Site
Pembroke Street
Cambridge, CB2 3RA
UK
E-mail: mk306@cam.ac.uk

Preprint No. 52

c4e

Key words and phrases: PAH, soot, aromatic site, kinetic Monte Carlo, simulation, modelling

Edited by
Cambridge Centre for Computational Chemical Engineering
Department of Chemical Engineering
University of Cambridge
Cambridge CB2 3RA
United Kingdom.

Fax: + 44 (0)1223 334796
E-Mail: c4e@cheng.cam.ac.uk
World Wide Web: http://www.cheng.cam.ac.uk/c4e/

Abstract

A detailed PAH growth model is developed, which is solved using a kinetic Monte Carlo algorithm. The model describes the structure and growth of planar PAH molecules, and is referred to as the kinetic Monte Carlo—aromatic site (KMC-ARS) model. A detailed PAH growth mechanism based on reactions at radical sites available in the literature, and additional reactions obtained from quantum chemistry calculations are used to model the PAH growth processes. New rates for the reactions involved in the cyclodehydrogenation process for the formation of 6-member rings on PAHs are calculated in this work based on density functional theory simulations. The KMC-ARS model is validated by comparing experimentally observed ensembles on PAHs with the computed ensembles for a C_2H_2 and a C_6H_6 flame at different heights above the burner. The motivation for this model is the development of a detailed soot particle population balance model which describes the evolution of an ensemble of soot particles based on their PAH structure. However, at present incorporating such a detailed model into a population balance is computationally unfeasible. Therefore, a simpler model referred to as the site-counting model has been developed, which replaces the structural information of the PAH molecules by their functional groups augmented with statistical closure expressions. This closure is obtained from the KMC-ARS model, which is used to develop correlations and statistics in different flame environments which describe such PAH structural information. These correlations and statistics are implemented in the site-counting model, and results from the site-counting model and the KMC-ARS model are in good agreement. Additionally the effect of steric hinderance in large PAH structures is investigated and correlations for sites unavailable for reaction are presented.

Contents

1 Introduction

There is general consensus in the literature that soot particles are formed of polycyclic aromatic hydrocarbons (PAHs), the growth of which is directly linked to the formation of soot particles [20]. The smallest aromatic compound, benzene, is believed to be formed by aliphatic molecules and radicals [32] that are generated by the pyrolysis of fuel molecules [25]. Once benzene forms, it is believed to grow to form larger PAHs [25] by the hydrogen-abstraction—carbon-addition (HACA) mechanism [23]. This mechanism involves PAH growth by the addition of acetylene (C_2H_2) at aromatic radical sites.

To determine the geometry of PAHs present in soot particles, a number of morphological studies have been conducted in the past on soot generated from different sources, like flames and engines [12, 55, 56]. These studies reveal that soot particles mainly consist of planar PAH molecules. It is well known that a soot particle is composed of primary particles linked together to form a fractal aggregate [17, 58]. High Resolution Transmission Electron Microscopy (HRTEM) images of soot particles show that the primary particles are near-spherical in shape, and are crystalline near the outer edge. This crystallinity arises due to stacking of planar PAHs to form parallel atomic layers and their alignment along the periphery of primary particles [12, 34, 55, 56]. However, the nuclei of primary particles are amorphous in nature. The presence of non-crystalline nuclei is evident from the experimental findings of Vander Wal et al. [58]. HRTEM images of partially oxidised soot particles were observed in [58], which show hollow centers, indicating the presence of amorphous and thus more reactive carbon sheets in the center of the primaries. This amorphous nature arises from the random orientation of PAHs inside the nuclei [58]. Braun et al. [8] observed soot particles from diesel engines in various conditions and concluded that the amount of crystallites (stacked graphene sheets or planar PAHs) always exceeds the amount of randomly oriented PAHs in diesel soot. A study on morphology of soot particles from different fuels was conducted by Vander Wal and Tomasek [57]. It was concluded that the degree of crystallinity depends on the fuel being pyrolysed to produce soot. The degree of crystallinity was highest in soot from the pyrolysis of acetylene as compared to soot from benzene and ethanol. The PAHs or graphene sheets present in soot from acetylene and benzene were planar. However, the PAHs present in soot from ethanol were observed to have curvature.

There is experimental evidence that shows the presence of substructures in primary particles [8, 17, 34]. In [17], HRTEM images of soot particles in a propane flame were observed, and the authors believe that a soot particle is composed of three kinds of nanostructures: primary particles forming chain-like aggregates; sub-primary particles having ellipsoidal shape and clustered to form small chains of less than 10 subunits; and elementary particles having shell-like structures with outer edge composed of amorphous carbon. Elementary particles were believed to form the inner graphitic nuclei of soot particles. In [34], the spherical substructures in the center of primary particles were designated as inner core and fine particles. Several layers of PAHs having bending structures were observed around the fine particles, indicating the involvement of non-planar PAHs having embedded 5-member rings [33] in soot nucleation. In their work as well, the outer layer of soot was observed to have graphitic crystallites, which may undergo polycyclic growth due to molecules, ions or radicals with two to four carbon atoms [34]. In brief, the above

experimental findings on soot morphology suggest that the outer edge of soot particles mainly consists of crystalline stacks of planar PAHs, and therefore, surface growth of a soot particle takes place through the growth of PAHs present in those crystalline stacks.

Current soot models consider the processes of inception, surface growth and coagulation of soot particles. The model referred to as the ABF model [3, 23] is commonly used to describe soot formation in flames and other systems, though it must often be augmented to match experimental observations [15, 65]. Soot mass is generated by the inception and surface growth processes, though it is believed that the majority of the soot mass comes from surface growth reactions [31]. The ABF model only includes one C_2H_2 addition reaction which contributes to surface growth, the rate of which is estimated for the rate of C_2H_2 addition at armchair sites (defined later). Frenklach et al. [19, 27] have presented a more complete soot surface growth model which includes C_2H_2 at different surface sites, as well as ring desorption, however, this model has not been implemented in population balances and has only been used to simulate the growth of graphene sheets. Thus, it appears that the present ABF soot model is incomplete and lacks a number of important reaction steps, by which a soot particle can grow. It has been certainly observed in the past that the ABF soot model underpredicts the soot volume fraction in flames [45, 51, 67].

A number of refinements to the PAH and soot growth model have been proposed [27, 61], which allows a soot particle to be represented by its constituent PAHs. An advantage of tracking the shape of constituent PAHs is that the reactive site density (and types) on soot particles can be exactly known, rather than estimated [23]. The PAH growth model presented by Violi [59] models large, non-planar PAH sheets in a flame-like environment. A large set of reactions, including 5-member ring formation, is used to describe the growth of a PAH molecule, using a kinetic Monte Carlo (KMC) algorithm and molecular dynamics (MD) calculations [61]. An optimized PAH molecule geometry is generated. The study by Keller et al. [39] showed that fullerenes and PAHs that exist independently in flames develop 3D structures, which motivated the KMC-MD model of Violi et al. [61]. This model describes single-atomic layer PAHs, which are present towards the beginning of the flame, and which are assumed to be involved in soot nucleation. Frenklach et al. [19, 27] proposed a PAH growth model, by which a planar graphene structure is allowed to grow only in one particular direction. The assumption of planar structure of PAHs is in agreement with the experimental findings about the composition of soot particles (stated above) in the later stages of soot growth.

With current computing resources, the simulation of the detailed PAH growth models is either very computationally expensive [35], or involves restrictive assumptions [27]. The inclusion of such detailed models into particle population balances is also prohibitively computationally expensive, however, a method for inclusion of such detailed PAH models into particle population balances has been recently published [9]. The site-counting model was presented which does not store the structural information of the PAHs present in soot particles, but rather estimates the structure by counting the number of each type of surface site and by using correlations and statistics to describe their interaction.

The aim of this paper is to present a detailed PAH growth model, referred to as the kinetic Monte Carlo—aromatic site (KMC-ARS) model, which stores the structural information of a PAH molecule as it grows in a flame-like environment. The model is solved using a kinetic Monte Carlo algorithm. A large set of soot surface processes reported in the liter-

ature [9, 27, 44, 59, 60], including oxidation processes [9], has been used for the model development. A recently calculated rate for O_2 oxidation of PAHs [10] has been employed in this study. New rates for the reactions involved in the cyclodehydrogenation process for the formation of 6-member rings on PAHs have been calculated in this work based on density functional theory simulations at HCTH407 level of theory. The KMC-ARS model has been validated by comparing the PAH ensembles observed experimentally for a C_2H_2 flame [64] and a C_6H_6 flame [39] with the computed ensembles at different heights above the burner. A statistical method has been presented which allows the structure of the resultant PAHs to be described by simple, rapidly computed, expressions, which make it possible to incorporate this advanced model into a particle population balance to account for surface growth of soot particles for the first time [9]: the site-counting model. The site-counting model is computationally very cheap, and can be included easily in a soot particle population balance. A detailed description of the methods employed to obtain statistics and correlations is provided. A study on the variation of PAH statistics with flame properties like type of fuel, cold gas velocity, C/O ratio and pressure has been conducted. The correlations and statistics are provided for commonly observed premixed laminar flames to make their simulations possible using the site-counting model. A comparison between the KMC-ARS and site-counting models is discussed.

2 ARS Model

In a previous paper [9] a detailed PAH model was developed, whereby PAHs are described by their reactive sites. A PAH molecule is assumed to be fully described by three major characteristics: the number of carbon (C) atoms, number of hydrogen (H) atoms, and the number of reactive sites. A discussion of reactive sites has been given previously by Celnik et al. [9], and is reviewed here. A site is a structure present on the outer edge of PAHs formed by two consecutive surface carbon atoms (those carbon atoms having bonded H atoms). The sites are differentiated by the number of carbon atoms required for their formation. Simple PAH geometry requires that a site has exactly two surface carbon atoms, and zero to four bulk carbon atoms (carbon atoms not having a bonded H atom). In this way four elementary sites can be defined, which are shown in figure 1: free-edges, zig-zags, armchairs and bays. Additionally, a 5-member ring may occupy a zig-zag site [27], therefore these have also been included in this model. PAH geometry also requires that, for a closed loop, each site must have two neighbouring sites. This is an important consideration as, in general, surface processes at one site will affect at least two other sites.

In this paper, a number of site terminologies are used, which are defined here:

- Elementary sites: The sites in figure 1 are called elementary sites.
- Combined sites: These sites are formed by more than one consecutive elementary site.
- Parent site: The site on which a chosen reaction takes place. This site gets replaced in the reaction.

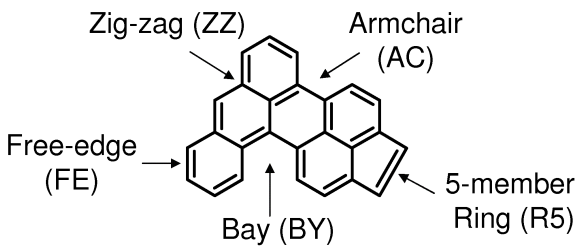

Figure 1: *An example PAH showing the principal surface site types.*

- Neighbour sites: In a reaction on a parent site, the two sites present on the either side of the parent site are called neighbour sites. After a reaction, neighbour sites change their types in a defined way.

2.1 PAH Reactions

In the literature, a large number of reactions by which a PAH molecule can grow are available [9, 27, 44, 59, 60]. Celnik et al. [9] have collected an extensive set of PAH reactions along with their rate constants at a pressure of 101.3 kPa, which are required to develop the PAH growth mechanism. The present work involves PAH growth simulations at two different pressures: 2.67 kPa and 101.3 kPa. For the simulation at 101.3 kPa, the set of reactions provided in Celnik et al. [9] was used. A literature survey was undertaken to obtain the rate constants for the PAH reactions at a pressure of 2.67 kPa, and a list of elementary reactions along with their Arrhenius rate constants and references are provided in table 1. More than one set of rate constants for some of the reactions at the same pressure were available in the literature, which varied significantly from one another, and are listed in the same table. For reactions 7, 9 and 10, rate constants were available for aromatic species with different number of rings, like benzene, naphthalene, phenanthrene and pyrene. For such reactions, the rate constants evaluated for aromatic species with highest number of rings were used in this work.

In table 1, different symbols have been used to represent the sites present on the edge of a PAH molecule, and are explained below:

$\mathrm{C_s^\bullet}$	A radical site	$\mathrm{C_sR5}$	5-member ring
$\mathrm{C_{s,fe}R6}$	6-member ring occupying a FE site	$\mathrm{C_{s,fe}R5}$	R5 next to FE
$\mathrm{C_{s,zz}R5}$	R5 next to ZZ	$\mathrm{C_{s,ac}R5}$	R5 next to AC
$\mathrm{C_{s,ac}R6}$	6-member ring next to AC	$\mathrm{C_{s,i}}$	PAH with i number of rings
$\mathrm{C_s(eR5)}$	Embedded R5 ring on PAH edge		

It can be noticed that a number of reactions involve adjacent elementary sites (combined sites).

Table 1: *PAH Surface Reactions. The rate constants are of the form:* $\mathrm{AT^n\,exp(-E/RT)}$*, and at a pressure of 2.67 kPa.*

No.	Reaction	A^a	n	E^a	Ref.
Hydrogen abstraction from, and addition to free-edges, zig-zags and armchairs					
1	$C_s - H + H \rightleftharpoons C_s^\bullet + H_2$	3.23×10^{07}	2.095	15.84	[42, 47, 49]
-1a	$C_s^\bullet + H_2 \rightleftharpoons C_s + H$	3.90×10^{12}		46.00	[40]
-1b	$C_s^\bullet + H_2 \rightleftharpoons C_s + H$	3.40×10^{09}	0.880	7.871	[19]
-1c	$C_s^\bullet + H_2 \rightleftharpoons C_s + H$	3.90×10^{12}		9.330	[36]
2a	$C_s^\bullet + H \rightarrow C_s$	3.49×10^{39}	−7.770	13.37	[24]
2b	$C_s^\bullet + H \rightarrow C_s$	8.02×10^{19}	−2.011	1.968	[43, 47, 49]
3	$C_s - H + OH \rightleftharpoons C_s^\bullet + H_2O$	2.10×10^{13}		19.10	[24]
-3	$C_s^\bullet + H_2O \rightleftharpoons C_s - H + OH$	3.68×10^{08}	1.139	17.10	[24]
Hydrogen abstraction from, and addition to, 5-member rings					
4	$C_sR5 + H \rightleftharpoons C_sR5^\bullet + H_2$	5.07×10^{07}	1.930	12.95	[41, 47, 49]
-4a	$C_sR5^\bullet + H_2 \rightleftharpoons C_sR5 + H$	3.01×10^{04}	2.630	8.540	[50, 53]
-4b	$C_sR5^\bullet + H_2 \rightleftharpoons C_sR5 + H$	1.57×10^{11}		5.260	[2, 50]
-4c	$C_sR5^\bullet + H_2 \rightleftharpoons C_sR5 + H$	9.46×10^{03}	2.560	5.060	[41]
5	$C_sR5^\bullet + H \rightarrow C_sR5$	1.40×10^{30}	−3.860	3.320	LP limit [52] [b]
		6.08×10^{12}	0.270	0.280	HP limit [52] [b]
6	$C_sR5 + H \rightleftharpoons C_sR5H^\bullet$	8.42×10^{08}	1.490	0.990	[47, 49, 53] [c]
-6	$C_sR5H^\bullet \rightleftharpoons C_sR5 + H$	6.28×10^{37}	−8.240	44.67	[24] [d]
Free-edge ring growth					
7a	$C_s^\bullet + C_2H_2 \rightleftharpoons C_sC_2H_2^\bullet$	7.70×10^{40}	−9.190	13.40	[62]
7b	$C_s^\bullet + C_2H_2 \rightleftharpoons C_sC_2H_2^\bullet$	4.40×10^{49}	−11.60	19.30	[62]
8a	$C_sC_2H_2^\bullet \rightleftharpoons C_sC_2H + H$	2.74×10^{22}	−4.061	37.04	[47, 49]
8b	$C_sC_2H_2^\bullet \rightleftharpoons C_sC_2H + H$	4.30×10^{51}	−12.19	48.00	[62]
9a	$C_s^\bullet + C_2H_2 \rightleftharpoons C_sC_2H + H$	7.50×10^{26}	−3.960	17.10	[62]
9b	$C_s^\bullet + C_2H_2 \rightleftharpoons C_sC_2H + H$	8.00×10^{17}	−1.210	22.60	[62]
9c	$C_s^\bullet + C_2H_2 \rightleftharpoons C_sC_2H + H$	1.40×10^{22}	−2.640	17.40	[62]
9d	$C_s^\bullet + C_2H_2 \rightleftharpoons C_sC_2H + H$	1.70×10^{30}	−4.960	20.50	[62]
10a	$C_s^\bullet C_2H + C_2H_2 \rightleftharpoons C_s(C_2H)C_2H_2^\bullet$	3.90×10^{48}	−11.30	27.20	[62]
10b	$C_s^\bullet C_2H + C_2H_2 \rightleftharpoons C_s(C_2H)C_2H_2^\bullet$	8.56×10^{44}	−10.50	13.22	[62]
11a	$C_s(C_2H)C_2H_2^\bullet \rightarrow C_sR6^\bullet$	2.50×10^{12}	−0.130	15.72	[9]
11b	$C_s(C_2H)C_2H_2^\bullet \rightarrow C_sR6^\bullet$	2.93×10^{60}	−14.99	24.40	[24] [e]
Free-edge ring desorption					
12	$C_{s,fe}R6^\bullet \rightleftharpoons C_s(C_2H)C_2H_2^\bullet$	1.60×10^{05}			[16], 1500 K. [f]
		1.50×10^{07}			[16], 2000 K.
		1.20×10^{08}			[16], 2500 K.
13	$C_{s,fe}(C_2H)C_2H_2^\bullet \rightleftharpoons C_s^\bullet C_2H + C_2H_2$	5.74×10^{56}	−13.12	16.62	[62] [g]
14	$C_{s,fe}^\bullet C_2H + H \rightarrow C_sC_2H$	same as reaction 2			[16]
15	$C_sC_2H + H \rightleftharpoons C_sC_2H_2^\bullet$	1.80×10^{25}	−4.500	4.200	[62]
16	$C_sC_2H_2^\bullet \rightleftharpoons C_s^\bullet + C_2H_2$	1.83×10^{46}	−10.46	13.17	[62] [g]
5-member ring addition to zig-zags					
17	$C_s^\bullet + C_2H_2 \rightarrow C_sR5 + H$	4.00×10^{13}		10.12	[24]
5-member ring desorption					
18	$C_sR5^\bullet \rightarrow C_sC_2H^\bullet$	1.60×10^{14}		177.5	[26]
Armchair ring growth					
19	$C_s^\bullet + C_2H_2 \rightleftharpoons C_sC_2H_2^\bullet$	6.70×10^{45}	−10.55	21.2	[62]
One step armchair ring growth (ABF model)					
20a	$C_s^\bullet + C_2H_2 \rightarrow C_sR6 + H$	1.87×10^{07}	1.787	3.262	[47, 49]
20b	$C_s^\bullet + C_2H_2 \rightarrow C_sR6 + H$	3.98×10^{13}		10.10	[18, 48]
20c	$C_s^\bullet + C_2H_2 \rightarrow C_sR6 + H$	4.00×10^{23}	−3.20	14.40	[62]

No.	Reaction	A	n	E^a	Ref.
5-member ring migration					
21	$C_{s,zz}R5H^\bullet \rightarrow C_sR5 + H$	5.63×10^{11}			[27], 1500 K.
		1.02×10^{12}			[27], 2000 K.
		1.13×10^{12}			[27], 2300 K.
5- to 6-member ring conversion at free-edges ([27])					
22	$C^\bullet_{s,fe}(R5H^\bullet) + C_2H_2 \rightleftharpoons C_s(R5H^\bullet)C_2H_2{}^\bullet$	same as reaction 7			[19, 27]
23	$C^\bullet_{s,fe}(R5H^\bullet) + C_2H_2 \rightleftharpoons C_s(R5H^\bullet)C_2H + H$	same as reaction 9			[19, 27]
24	$C_{s,fe}(R5H^\bullet)C_2H \rightarrow C_sR6^\bullet$	same as reaction 11			[27]
6- to 5-member ring conversion at armchairs					
25	$C_{s,ac}R6^\bullet \rightarrow C_sR5^\bullet + C_2H_2$	same as reaction 12			[27]
5- to 6-member ring conversion at armchairs					
26	$C_{s,ac}R5H^\bullet \rightarrow C_sR6 + H$	5.63×10^{11}			[27], 1500 K.
		1.02×10^{12}			[27], 2000 K.
		1.13×10^{12}			[27], 2300 K.
Free-edge oxidation					
27a	$C_sR6^\bullet + O_2 \rightarrow C_sC_2H + HCO + CO$	2.20×10^{12}		31.40	[3]
27b	$C_sR6^\bullet + O_2 \rightarrow C_sC_2H + HCO + CO$	2.10×10^{12}		31.30	[63]
27c	$C_sR6^\bullet + O_2 \rightarrow C_sC_2H + HCO + CO$	9.70×10^{03}	2.42	38.48	[10]
28	$C_sR6 + OH \rightarrow C_sC_2H + CH_2CO$	1.30×10^{13}		44.40	[63]
29	$C_sC_2H + O \rightarrow C^\bullet_s + HCCO$	2.04×10^{07}	2.00	7.90	[63]
Armchair oxidation					
30a	$C^\bullet_{s,fe} + O_2 \rightarrow C^\bullet_s + 2CO$	2.20×10^{12}		31.40	[3]
30b	$C^\bullet_{s,fe} + O_2 \rightarrow C^\bullet_s + 2CO$	2.10×10^{12}		31.30	[63]
30c	$C^\bullet_{s,fe} + O_2 \rightarrow C^\bullet_s + 2CO$	9.70×10^{03}	2.42	38.48	[10]
31	$C_{s,fe} + OH \rightarrow C^\bullet_s + CHO + CH$	1.30×10^{13}		44.40	[3]
Benzene addition					
32a	$C_s{}^\bullet + C_6H_6 \rightleftharpoons C_sC_6H_5 + H$	1.90×10^{76}	−18.90	39.47	[47, 49]
32b	$C_s{}^\bullet + C_6H_6 \rightleftharpoons C_sC_6H_5 + H$	1.27×10^{05}			[44], 300 K.
		1.60×10^{08}			[44], 500 K.
		7.83×10^{09}			[44], 700 K.
		5.37×10^{10}			[44], 1000 K.
		8.43×10^{10}			[44], 1500 K.
		8.01×10^{09}			[44], 2000 K.
		1.62×10^{08}			[44], 2500 K.
5-member bay closure ([60])					
33	$C^\bullet_{s,\,i} \rightarrow C_{s,\,i+1} + H$	3.86×10^{11}	0.210	17.70	[60]
6-member bay closure ([54])					
34	$C_{s,\,i} + H \rightarrow C^\bullet_{s,\,i} + H_2$	9.24×10^{07}	1.50	9.646	this work, HCTH407[h]
		5.60×10^{07}	1.78	10.60	this work, B3LYP[h]
-34	$C^\bullet_{s,\,i} + H_2 \rightarrow C_{s,\,i} + H$	9.60×10^{04}	1.96	9.021	this work, HCTH407[h]
35	$C^\bullet_{s,\,i} \rightarrow C^\bullet_{s,\,i+1}H$	1.11×10^{11}	0.658	23.99	this work, HCTH407[h]
36	$C^\bullet_{s,\,i+1}H \rightarrow C_{s,\,i+1} + H$	1.44×10^{13}	−0.57	3.662	this work, HCTH407[h]
37	$C^\bullet_{s,\,i} \rightarrow C_{s,\,i+1} + H$	3.49×10^{12}	−0.39	2.440	this work, HCTH407[h]
Embedded 5-member ring migration to zig-zags ([60])					
38	$C^\bullet_s(eR5) \rightarrow C^\bullet_s(R5)$	4.96×10^{11}	0.755	50.0	[60]
39	$C^\bullet_s(R5) + H \rightarrow C_s(R5)$	2.33×10^{08}	1.390	−1.950	[60]

No.	Reaction	A	n	E^a	Ref.

[a] *The units are kcal, mol, cm and sec.*
[b] *Analogous to $C_2H_3 + H \rightarrow C_2H_4$ [27]. The rate constant for this reaction was calculated using the high-pressure and the low-pressure limit rate constants, and was expressed in Troe falloff form [28] as suggested in [52]. The parameters required to express the rate constant in Troe form were obtained from [52].*
[c] *Analogous to $C_2H_4 + H \rightarrow C_2H_5$. [27]*
[d] *Analogous to $C_2H_5 \rightarrow C_2H_4 + H$. [27]*
[d] *Analogous to n-$C_6H_5 \rightleftharpoons A1-$.*
[f] *Assumed to be same as decyclization of a phenyl radical.*
[g] *Calculated using equilibrium constant.*
[h] *Level of theory used for DFT calculations.*

2.1.1 Cyclodehydrogenation process

New rates for the reactions involved in the cyclodehydrogenation process leading to the formation of a 6-member ring on PAHs (6-member bay closure) have been evaluated using density functional theory (DFT) with the HCTH/407 functional. For this purpose, a theoretical study on the conversion of Benzo[ghi]perylene to Dibenzo[c,g]phenanthrene was conducted. A number of mechanisms are available in the literature for the cyclodehydrogenation process [54, 66]. In this study, a free-radical mechanism (table 2, process S14) has been taken from a theoretical investigation in the literature [54]. Additionally, a new route for the product formation has been suggested.

The HCTH/407 functional was fitted to a training set of 407 molecules including a large number of hydrocarbons by Boese and Handy [6]. This means it is especially well suited to the investigation of carbon-hydrogen systems. In order to verify the performance of this functional two further tests were performed. Firstly, the experimentally observed C-H bond dissociation energies (BDEs) of 113.9, 109.3 and 102.1 kcal/mol [30] were calculated with the HCTH/407 functional as 116.9 kcal/mol at T = 0 K. An error of 5-10% is adequate for the purposes of our model. The more accurate (and substantially slower) MP2/6-31G** level of theory predicts a BDE of 117.7 kcal/mol for instance [30]. The second validation involves comparing the energy required for the dehydrogenation of benzene ($C_6H_6 \rightarrow C_6H_4 + H_2$). The high-cost high-accuracy methods of MP2/6-311G**, QCISD/6-311G**, CCSD(T)/6-311G** and BLYP/6-311G** predict the energy required as 86.1, 91.2, 86.8 and 82.8 kcal/mol, respectively [14], whereas our calculations with HCTH/407 predict a value of 90.8 kcal/mol. A recent experimental report gives the required energy as 86.6 $\pm$ 3.0 kcal/mol at T = 298 K [60]. The level of prediction of experimental observations by the HCTH/407 functional provides adequate ground for its use for similar theoretical calculations on PAHs present in our molecular system.

Figure 2 shows the relative energies of all the chemical species and transition states involved in the mechanism at 0 K. The dashed lines in figure 2 show a new possible reaction path.

The calculated rate constants for the reactions involved in the mechanism are listed in table 1 (reactions 34–37). The rate constants for the reactions involved in this cyclodehydrogenation process were evaluated using transition state theory (TST). The partition

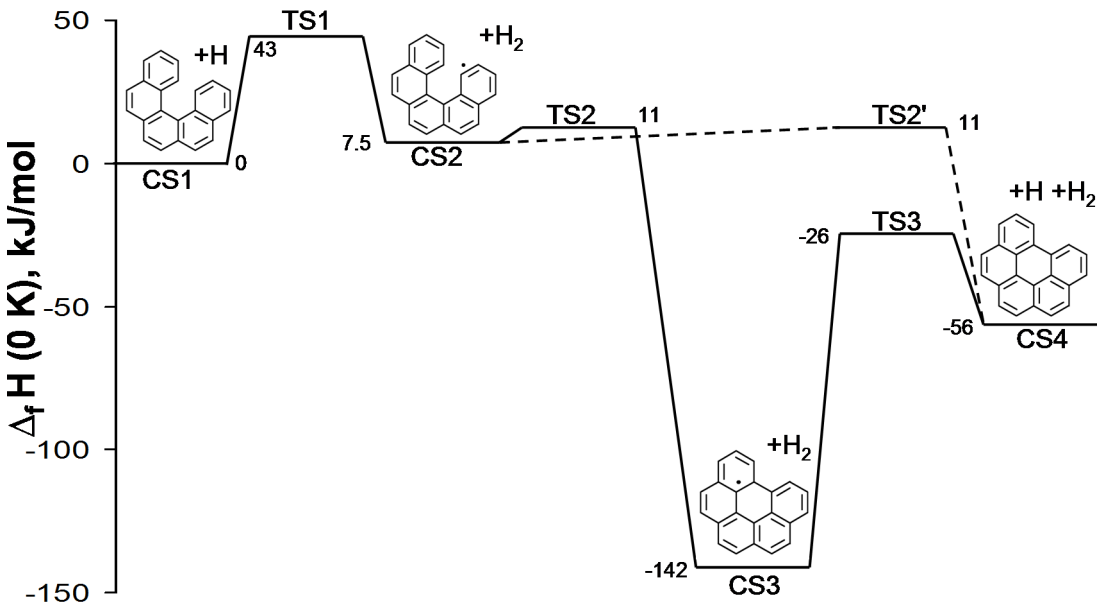

Figure 2: *A potential energy diagram showing energies of the chemical species (CS) and transition states (TS) for the cyclodehydrogenation of Benzo[ghi]perylene to Dibenzo[c,g]phenanthrene. Solid line represents the route proposed in [54]. Dashed line represents a route suggested in this work.*

functions for the transition state and reactants were calculated at a range of temperatures (300-3000 K) using the vibrational frequencies, moments of inertia, mass and electronic multiplicity, all of which are given by the quantum calculations. A linear least-square fitting algorithm was used to fit the modified Arrhenius expression:

$$k(T) = A \times T^n \times \exp\left(\frac{-E}{RT}\right) \tag{1}$$

to the data points of the rate constants in order to obtain the rate coefficients A, n and E. The rate constant for reaction 34 was also calculated using the B3LYP functional with a 6-31G* basis set, and is provided in table 1. This rate is very similar to that calculated using HCTH/407 and provides further support for the use of HCTH/407.

2.2 PAH processes

Table 2 shows a list of PAH processes involving 5-member and 6-member ring addition and removal, and oxidation of reactive sites. This list is based on the reactions provided in [9] amended with the reaction for bay closure studied in this work and some other reactions from the literature [21, 27, 44, 60]. The reaction mechanisms are provided in table 2 for only the newly added processes. For each process listed in this table, several intermediate species are involved in the reaction mechanism. If all the intermediate species present in the reaction mechanisms are considered, the simulation of a PAH molecule would become computationally very expensive. Therefore the intermediate species were

Route I [21]

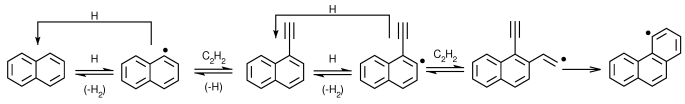

Route II [27]

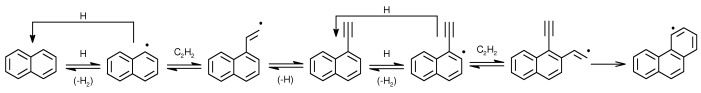

Figure 3: *Different pathways for free-edge growth.*

assumed to be in steady state, and that the ring addition and desorption steps are irreversible [9, 27]. A detailed explanation for these assumptions can be found in [9]. The PAH processes were then represented as jump processes (see table 2). The rate expressions for the jump processes obtained after the steady-state analysis are presented in the same table. In the rate expressions, the term $[\mathrm{C_S}]$ represents the concentration of parent site S. Appel et al. [3] argued that the hydrogen atom on armchair and bay radical sites can easily jump from one side to another [13]. This process will double the rate of PAH growth processes involving these sites, like armchair growth reaction and bay closure reactions. In the light of above argument, PAH growth simulations were carried out by doubling the rates of armchair growth and bay closure reactions.

In the literature, two different routes for the free-edge growth reaction are available, as shown in figure 3: Route I involves an intermediate species with a free-radical after the addition of $\mathrm{C_2H_2}$ in step 2 as suggested in [19]; Route II involves direct addition of $\mathrm{C_2H_2}$ with the removal of an H atom. It is for the first time that both the routes are included in a PAH growth mechanism. There can be two different ways to include the two routes in the PAH growth mechanism: (a) Considering free-edge growth via the two routes as two different growth processes. In this case, the two resulting jump processes will be identical, but will have different rates. (b) Combining the two routes to form a single reaction mechanism (as shown in table 2 for process S1). In this work, the second method was used to incorporate the two routes in the PAH growth processes as they were very similar to each other.

Table 2: *Monte-Carlo Jump Processes*

Process [Ref.]	Parent site
S1 Free-edge ring growth [19, 21]	**Free-edge**
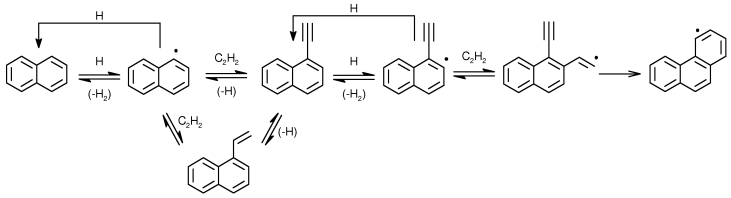	
Jump Process: 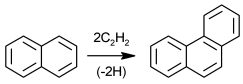	Rate: $(k_{7b} + k_{9b}) \left(\frac{k_1[\mathrm{H}]+k_3[\mathrm{OH}]}{k_{-1b}[\mathrm{H_2}]+k_{2a}[\mathrm{H}]+k_{-3}[\mathrm{H_2O}]+(k_{7b}+k_{9b})[\mathrm{C_2H_2}]} \right) [\mathrm{C_2H_2}][\mathrm{C_{fe}}]$

Process [Ref.]	Parent site
S2 Armchair ring growth [3, 9]	**Armchair**
Jump Process: 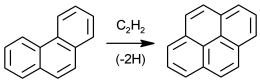	Rate: $k_{20a}\left(\frac{k_1[\mathrm{H}]+k_3[\mathrm{OH}]}{k_{-1b}[\mathrm{H_2}]+k_{2a}[\mathrm{H}]+k_{-3}[\mathrm{H_2O}]+k_{20a}[\mathrm{C_2H_2}]}\right)[\mathrm{C_2H_2}][\mathrm{C_{ac}}]$
S3 Free-edge ring desorption [9, 19]	**6-member ring**
Jump Process: 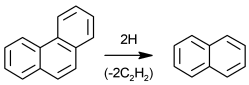	Rate: $k_{12}\left(\frac{k_1[\mathrm{H}]+k_3[\mathrm{OH}]}{k_{-1b}[\mathrm{H_2}]+k_{2a}[\mathrm{H}]+k_{-3}[\mathrm{H_2O}]+k_{12}}\right)[\mathrm{C_{fe}R6}]$
S4 6- to 5-member ring conversion at armchair [9, 27]	**6-member ring next to armchair**
Jump Process: 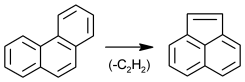	Rate: $k_{25}\left(\frac{k_1[\mathrm{H}]+k_3[\mathrm{OH}]}{k_{-1b}[\mathrm{H_2}]+k_{2a}[\mathrm{H}]+k_{-3}[\mathrm{H_2O}]+k_{25}}\right)[\mathrm{C_{ac}C_{fe}R6}]$
S5 5-member ring addition [9, 26]	**Zig-zag**
Jump Process: 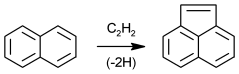	Rate: $k_{17}\left(\frac{k_1[\mathrm{H}]+k_3[\mathrm{OH}]}{k_{-1b}[\mathrm{H_2}]+k_{2a}[\mathrm{H}]+k_{-3}[\mathrm{H_2O}]+k_{17}[\mathrm{C_2H_2}]}\right)[\mathrm{C_2H_2}][\mathrm{C_{zz}}]$
S6 5-member ring desorption [9, 26]	**5-member ring**
Jump Process: 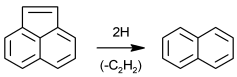	Rate: $k_{18}\left(\frac{k_4[\mathrm{H}]}{k_{-4c}[\mathrm{H_2}]+k_5[\mathrm{H}]+k_{18}}\right)[\mathrm{C_{zz}R5}]$
S7 5- to 6-member ring conversion at free edge [27]	**5-member ring next to free-edge**
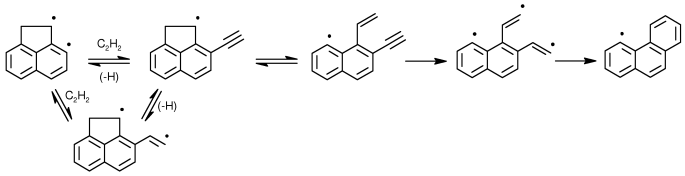	
Jump Process: 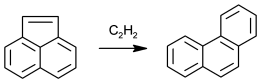	Rate: $(k_{7b}+k_{9b})\left(\frac{k_6[\mathrm{H}]}{k_{-6}+f}\right)f[\mathrm{C_2H_2}][\mathrm{C_{fe}R5}]$, where $f=\left(\frac{k_1[\mathrm{H}]+k_3[\mathrm{OH}]}{k_{-1b}[\mathrm{H_2}]+k_{2a}[\mathrm{H}]+k_{-3}[\mathrm{H_2O}]+(k_{7b}+k_{9b})[\mathrm{C_2H_2}]}\right)$
S8 5- to 6-member ring conversion at armchair [9, 27]	**5-member ring next to armchair**
Jump Process: 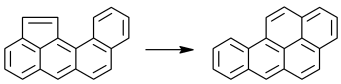	Rate: $k_{26}\left(\frac{k_6[\mathrm{H}]}{k_{-6}+k_{26}}\right)[\mathrm{C_{ac}R5}]$

Process [Ref.]	Parent site
S9 Free-edge oxidation by O_2 [9, 63]	**6-member ring**

Jump Process:

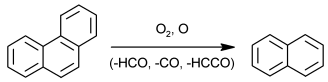

Rate:

$$k_{27c}\left(\frac{k_1[\mathrm{H}]+k_3[\mathrm{OH}]}{k_{-1b}[\mathrm{H_2}]+k_{2a}[\mathrm{H}]+k_{-3}[\mathrm{H_2O}]+k_{27c}[\mathrm{O_2}]}\right)[\mathrm{O_2}][\mathrm{C_{fe}R6}]$$

S10 Free-edge oxidation by OH [9, 63] — **6-member ring**

Jump Process:

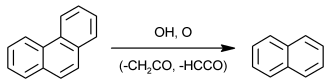

Rate:

$$k_{28}[\mathrm{OH}][\mathrm{C_{fe}R6}]$$

S11 Armchair oxidation by O_2 [9, 63] — **Free-edge**

Jump Process:

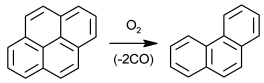

Rate:

$$k_{30c}\left(\frac{k_1[\mathrm{H}]+k_3[\mathrm{OH}]}{k_{-1b}[\mathrm{H_2}]+k_{2a}[\mathrm{H}]+k_{-3}[\mathrm{H_2O}]+k_{30c}[\mathrm{O_2}]}\right)[\mathrm{O_2}][\mathrm{C_{fe}}]$$

S12 Armchair oxidation by OH [9, 63] — **Free-edge**

Jump Process:

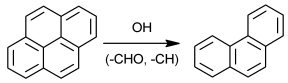

Rate:

$$k_{31}[\mathrm{OH}][\mathrm{C_{fe}}]$$

S13 Benzene addition [44] — **All site types**

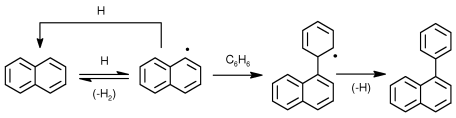

Jump Process:

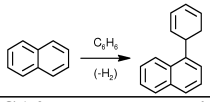

Rate:

$$k_{32a}\left(\frac{k_1[\mathrm{H}]+k_3[\mathrm{OH}]}{k_{-1b}[\mathrm{H_2}]+k_{2a}[\mathrm{H}]+k_{-3}[\mathrm{H_2O}]+k_{32a}[\mathrm{C_6H_6}]}\right)[\mathrm{C_6H_6}][\mathrm{C_s}]$$

S14 5-member ring migration [27] — **5-member ring next to zig-zag**

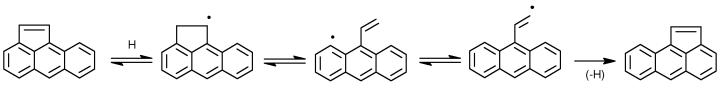

Jump Process:

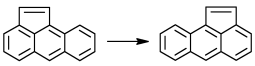

Rate:

$$k_{21}\left(\frac{k_6[\mathrm{H}]}{k_{-6}+k_{21}}\right)[\mathrm{C_{zz}R5}]$$

S15 6-member bay closure [7] — **6-member bay**

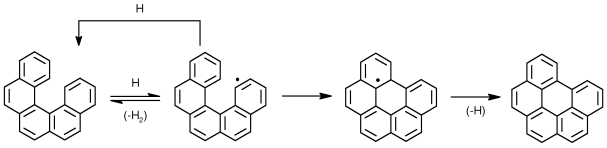

Jump Process:

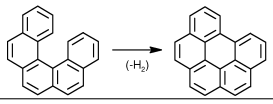

Rate:

$$k_{36}\left(\frac{k_{34}[\mathrm{H}]+k_3[\mathrm{OH}]}{k_{-34}[\mathrm{H_2}]+k_{2a}[\mathrm{H}]+k_{-3}[\mathrm{H_2O}]+k_{36}}\right)[\mathrm{C_{BY}}]$$

Process [Ref.]	Parent site
S16 5-member bay closure [60]	**5-member bay**
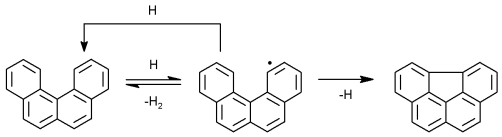	
Jump Process: 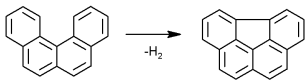	Rate: $k_{33}\left(\frac{k_1[\mathrm{H}]+k_3[\mathrm{OH}]}{k_{-1b}[\mathrm{H_2}]+k_{2a}[\mathrm{H}]+k_{-3}[\mathrm{H_2O}]+k_{33}}\right)[\mathrm{C_{BY}}]$
S17 Embedded 5-member ring migration to zig-zags [60]	**Embedded 5-member ring next to two adjacent free-edges**
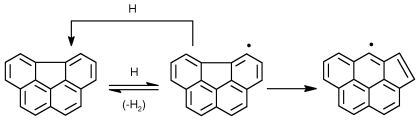	
Jump Process: 	Rate: $k_{38}\left(\frac{k_1[\mathrm{H}]+k_3[\mathrm{OH}]}{k_{-1b}[\mathrm{H_2}]+k_{2a}[\mathrm{H}]+k_{-3}[\mathrm{H_2O}]+k_{34}}\right)[\mathrm{C_{fe,fe}eR5}]$

3 KMC-ARS Model

In this paper a KMC algorithm has been developed to simulate the growth of single PAH molecules. KMC allows the structure of the growing PAH molecule to be tracked explicitly, hence no assumptions are required about the shape of the structure. However, this method is computationally expensive, and can currently only be used to simulate single molecules in reasonable computation times. The model is formulated mathematically in terms of the state-space and the jump processes (and their rates). In order to create an efficient numerical algorithm a higher level data structure is also defined, on which the jump processes are more easily described.

3.1 State Space

Tracking the structure of a PAH requires knowledge about the position of the C atoms and the bonds between them. As a PAH has a similar structure to graphite, it is clear that the bulk C atoms must bond with three others (not differentiating between single and double bonds), while surface C atoms form chemical bonds with two other C atoms and possibly a H atom. Thus, the simplest state space required to track the structure of the PAH molecule includes the following information: the positions of the C atoms, and the information about the bonds associated with the C atoms. The latter information is stored in terms of the positions of the other C atoms to which a C atom is bonded. For 2D representation of PAHs with planar or near-planar geometry [29], the state space E can

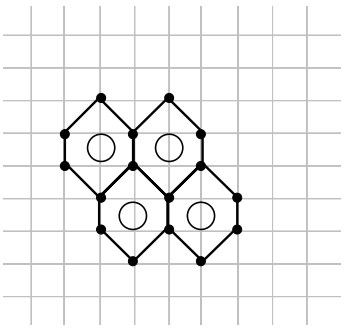

Figure 4: *An example grid showing a pyrene molecule.*

be represented as:

$$E = (i,\ j,\ i_1,\ j_1,\ i_2,\ j_2,\ i_3,\ j_3) \in \mathbb{Z}^8 \tag{2}$$

where $(i,\ j)$ are the coordinates of a C atom, and $(i_n,\ j_n)_{n=1,\ 2,\ 3}$ are the coordinates of the surrounding C atoms bonded to the C atom at $(i,\ j)$. For a surface C atom, $(i_3,\ j_3)$ is not defined, and is set to a predefined value, thus providing a method to differentiate a surface C atom from a bulk C atom. This state space includes all the possible states/structures adoptable by a PAH molecule. It would also be possible to generalise this state space further to 3D, by including additional coordinates and defining them in the set of real numbers.

While this state space is sufficient to fully define a PAH structure, definition of the Monte-Carlo jump processes on it is very difficult. Therefore, in order to simplify the problem, a higher order data structure is defined using the above state space, and the jump are defined using this data structure, which are described in the next section.

3.2 Data Structure

In this study, to track the PAH structure, a 2D grid is generated and the starting PAH molecule is placed on it such that each C atom is assigned a grid point. Figure 4 shows an example grid with a pyrene molecule. This 2D grid does not store the actual C-C bond lengths, however, this is acceptable as the bonds are implicitly represented in the rate expressions by the surface sites. Therefore, if the PAH molecule represented on a 2D grid is not present in any stack, it may develop a non-planar geometry.

Two vectors are defined using the above state space to describe this problem: a carbon atom vector c, and a site vector s. The vector c stores the following information: the two site types of which the C atom is a part, S_1 and S_2, the site indices (each site of a particular type is differentiated from others based on its index), S_{in_1} and S_{in_2}, the carbon atom type (bulk or surface), C_{type}, and its spatial coordinates, i and j. Thus, c can be represented as:

$$c = (S_1,\ S_2,\ S_{in_1},\ S_{in_2},\ C_{type},\ i,\ j) \in \mathbb{Z}^7$$

A site requires two surface C atoms, and all the required information about a site can be obtained from these C atoms. However, the derivation of site information from the carbon atoms allows the jump processes to be easily defined, but requires some duplication of information. Therefore, a site vector s was employed to store the following information: site type, S_{type}, site index (explained above), S_{in}, and the coordinates of the two surface C atoms, $(i_1,\ j_1)$ and $(i_2,\ j_2)$. Therefore, s can be represented as:

$$s = (S_{type},\ S_{in},\ i_1,\ j_1,\ i_2,\ j_2) \in \mathbb{Z}^6$$

The PAH structure is then fully described by the data structure e:

$$e = (c, s) \tag{3}$$

3.3 Jump Processes

The jump processes listed in table 2 are defined on sites of a particular type (parent sites). The information stored in vector s is used to define the rate (R_i) of jump process i using the equation:

$$R_i \quad = \quad k_i \times f_i \times C \times N_{site}(e) \tag{4}$$

where k_i is the Arrhenius rate constant of the form $AT^n e^{-E_a/RT}$ (listed in table 1), f_i is the fraction of radical sites of the parent type, found using the steady-state assumption [9], C is the concentration of the gas-phase species involved in the reaction and $N_{site}(e)$ is the number of parent sites on the structure, and is obtained from the data structure e. The expressions for the rate constants of intermediate reactions and the fraction of radical sites of the parent type can be obtained from tables 1 and 2.

On simulation of a jump the vectors c and s must be updated to reflect the changes to the PAH structure. Processes may add or remove C atoms, which must be reflected in the c vector, and the parent site will usually be destroyed. Additionally, the neighbour sites must also be updated in the s vector.

3.4 KMC Algorithm

The KMC algorithm used to track the growing structure is described below. This algorithm updates the PAH structure by removing the used sites and carbon atoms and adding the newly formed ones after each reaction.

1. Set $t \leftarrow 0$.
2. Initialise 2D starting structure by providing all the required information (figure 4): $e \leftarrow e_0$, where $e_0 \in E$.

3. Calculate the jump rates:

$$R_i = k_i \times f_i \times C \times N_{site}, \qquad i = 1, 2 \ldots I$$

where I is the number of processes in table 2.

4. Generate an exponentially distributed waiting time τ with parameter λ, where λ is the sum of all the jump rates:

$$\lambda = \sum_{i=1}^{I} R_i$$

5. Update $t \leftarrow t + \tau$

6. If $t \geq t_{stop}$, then END.

7. Choose a reaction based on the probability calculated using its reaction rate.

8. Uniformly select a site of correct type (table 2) and determine the positions of the two surface C atoms.

9. If ring addition reaction, determine the positions of the C atoms to be added and go to step 11.

10. If ring desorption reaction, go to step 13.

11. If the site is hindered by surrounding C atoms then go to step 3.

12. Update $e \in E$ according to reaction (table 2).

13. Update neighbour sites:

    (a) 6-member ring: For an addition reaction, change the neighbour site type by moving it ahead in the one of the following lists (depending on whether 0 or 1 five-member ring is involved): $\{FE \rightarrow ZZ \rightarrow AC \rightarrow BY\}$ or $\{R5FE \rightarrow R5ZZ \rightarrow R5AC \rightarrow R5BY\}$. For a desorption reaction, move back in one of the above lists.

    (b) 5-member ring: For addition reaction, change the neighbour site type in the following way: For site $S \in \{FE,\ ZZ,\ AC,\ BY\}$, then $S \rightarrow R5S$ and $R5S \rightarrow R5SR5$. For desorption reaction, $R5S \rightarrow S$, and $R5SR5 \rightarrow R5S$.

14. Go to step 3.

3.5 Error Estimation

The random variation in the values of a variable with the simulation runs is an inherent property of a stochastic algorithm. To estimate the statistical fluctuation in the simulated result of a variable, L trial runs are generated. The empirical mean of the realisations of the random variable Y: $[y_1(t), y_2(t), \ldots, y_L(t)]$ is calculated, and is represented by $\bar{y}(t)$:

$$\bar{y}(t) = \frac{1}{L}\sum_{l=1}^{L} y_l(t) \tag{5}$$

An example of a random variable Y used in this work can be the number of 6-member rings ($\mathrm{N_{R6}}$). A method to obtain this variable is explained in section 6.1.1. The empirical variance, η is then calculated using equation 6:

$$\eta(t) = \frac{1}{L}\sum_{l=1}^{L} y_l^2(t) - [\bar{y}(t)]^2 \tag{6}$$

The half-width of the error bound about the average value is calculated using the central limit theorem (equation 7) with $a = 3.29$ for a confidence level of 99.9%.

$$\epsilon(t) = a\sqrt{\frac{\eta(t)}{L}} \tag{7}$$

The confidence interval for a variable, $y(t)$ is then represented by:

$$I = [\bar{y}(t) - \epsilon(t),\ \bar{y}(t) + \epsilon(t)] \tag{8}$$

4 Site-Counting Model

The site-counting model presented by Celnik et al. [9] determines the soot particle composition and PAH sites information, assuming soot surface to be formed by stacking together of planar PAHs. It preserves the information about reactive sites, but neglects the spatial structure of PAHs to make this model computationally very cheap. This model abridges the gap between computationally expensive kinetic Monte Carlo or molecular dynamics models and the simple spherical carbon soot particle models [4, 46, 51]. The motivation of this model was to produce as much information about the PAH structure of soot as possible, while keeping the computational expense low enough to simulate particle populations, rather than just single particles [9]. The state space required for this model is nine dimensional, and is given by [9]

$$E = (C, H, N_{FE}, N_{ZZ}, N_{AC}, N_{BY}, N_{R5}, S_a, N_{PAH})$$

where N_x is the number of site type x, C and H are the number of carbon and hydrogen atoms respectively, S_a is the surface area of the particle and N_{PAH} is the number of PAHs which make up the particle. Based on this state space, particle processes like, inception, jump processes representing surface growth, and coagulation, on each particle of type $x \in \mathrm{E}$ can be defined by ODEs of the following form:

$$\frac{dx}{dt} = F\left(x, N_{R6\_AC}, N_{R5FE}, N_{R5AC}, N_{R5ZZ}, N_{R6}, P_{S,m}\right) \tag{9}$$

where N_y is the number of combined-site type y in the particle (see figure 11 for combined sites on an example PAH), $P_{S,m}$ is the probability of a site type $S \in \{ED, ZZ, AC, BY\}$ to act as a neighbour site in a process with index $m \in \{1, \ldots, \text{number of processes in table 2}\}$. The terms N_y and $P_{S,m}$ in the function F are required to completely close the ODEs. It is clear that these terms require structural information about PAHs, and cannot be exactly determined if the PAH structure is not tracked. Therefore, a statistical method is developed using the KMC-ARS model for the equation closure, in which N_y and $P_{S,m}$ are expressed as functions of x, and are briefly explained below:

N_y: The combined sites (N_y) are involved in a number of reaction steps (S3, S4, S7–S10, S14 and S17) in table 2. In the site-counting model, since the relative positions of the sites are not tracked, the counts of combined sites, required to calculate the reaction rates, cannot be determined. Therefore, the site-counting model needs an approximation to the structure to be calculated. This structural information is obtained using the KMC-ARS model to find correlations for the combined sites (N_y) in terms of elementary sites involved in their formation. A method to obtain the correlations for the major combined sites is detailed in section 6.1.1.

$P_{S,m}$: As mentioned before, a reaction on a parent site affects more than one site at a time. Figure 5 shows how an armchair growth reaction on phenanthrene to form pyrene affects two free-edges (neighbour sites) along with an armchair site (parent site). In this example,

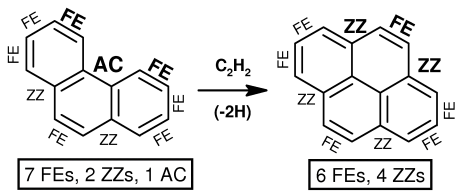

Figure 5: *An example of jump process S2. The site counts for both the molecules are provided. The affected sites are shown in bold face.*

the types of the neighbour sites were changed from free-edges to zig-zags. Thus, unless the structure of PAHs is tracked, it is not possible to exactly know the neighbour sites to be updated, when a reaction takes place on a parent site. The KMC-ARS model provides the information about the neighbour sites in different reactions in terms of weights to the counts of elementary sites. These weights are used to calculate $P_{S,m}$ and determine the neighbour sites in a PAH process in the site-counting model. A detailed explanation of the method used to obtain the site-weights and neighbour probabilities is provided in section 6.1.2.

A major advantage of site-counting model is that it is computationally very fast compared to the KMC-ARS model. A real-time KMC simulation of 2.4 ms for a PAH molecule takes about 1.5 seconds of computation time with the site-counting model and about 30 minutes with the KMC-ARS model in the same gas-phase environment.

Table 3: *Flame initial conditions*

Flame	Pressure (kPa)	Fuel	Composition (mole %)			Cold gas velocity (cm/sec)	$\frac{[C]}{[O]}$	Ref.
			Fuel	O_2	Ar			
1	2.67	C_2H_4	19.4	30.6	50	62.5	0.65	[5]
2	2.67	C_6H_6	70.6	29.4	0	42	0.8	[39]
3	2.66	C_2H_2	44.4	55.6	0	42	0.8	[64]
4	2.66	C_2H_2	50	50	0	42	1.0	[64]
5	2.66	C_2H_2	50	50	0	50	1.0	[64]
6	2.66	C_2H_2	51.4	48.6	0	42	1.06	[64]
7	2.67	C_2H_4	50	50	0	42	1.0	see text
8	101.3	C_2H_4	16.3	23.7	60	13	0.69	[1]
9	101.3	C_2H_4	16.3	23.7	60	10	0.69	[1]
10	101.3	C_2H_4	16.3	23.7	60	8	0.69	[1]
11	101.3	C_2H_4	16.3	23.7	60	6.53	0.69	[1]

5 Experimental validation

In this work, PAH growth simulations were carried out in several laminar premixed flames of C_2H_2, C_2H_4 and C_6H_6 to develop correlations revealing structural information of PAHs in different flame environments. Their variation with flame properties like type of fuel, cold gas velocity, C/O ratio and pressure was also studied. The operating conditions for these flames are provided in Table 3. In the literature, any experimental study on a C_2H_4–O_2 flame without any diluent at a pressure of 2.67 kPa was not available. Therefore, a hypothetical C_2H_4–O_2 flame (flame 7) was created for simulation, which uses the operating conditions of flame 4. All the flames were simulated using the ABF chemical mechanism [3] along with CHEMKIN package [38] and PREMIX [37] to obtain the chemical species profiles. Figure 6 shows the computed profiles of major chemical species for the flames 1, 2 and 4. In the literature, experimentally observed species profiles were available for flame 1 only and its comparison with the computed profiles is shown in figure 6(a). The growth of PAH molecules in all the flame environments was studied using the computed species profiles.

PAHs present in a low–pressure C_6H_6 flame (flame 2) and C_2H_2 flames (flames 3–6) have been observed experimentally in [39, 64] using Resonance Enhanced Multi-Photon Ionisation (REMPI) and time of flight–mass spectrometry (TOF-MS). The experimental details are briefly reviewed here. Ensembles of PAHs present in the gaseous phase at different heights above the burner (HAB) are collected. Neutral PAHs are ionised using REMPI, and the time of flight inside a flight tube is used to determine the mass of PAHs [33]. The observed ensemble of PAHs at a particular HAB is then represented on a C-H diagram, where each data point denotes a PAH with a fixed number of C and H atoms. In this work, the KMC-ARS model was validated by comparing the PAH ensembles obtained computationally with the experimentally observed ensembles represented

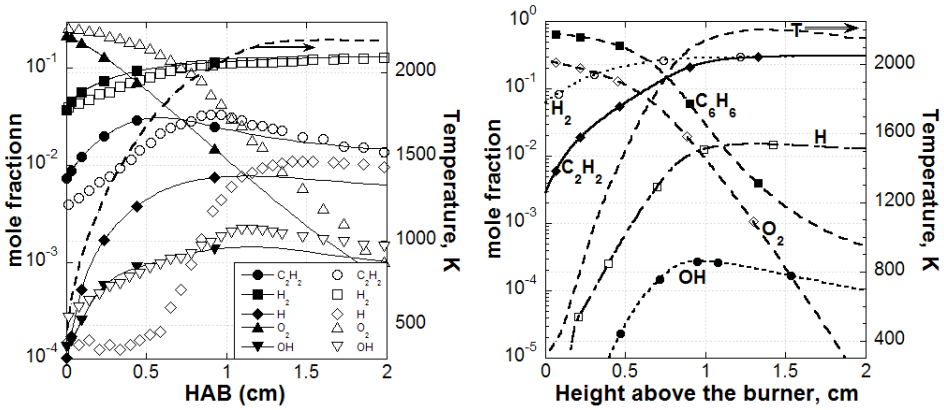

(a) C_2H_4 flame. Filled markers in the legend denote the computed species profiles and hollow markers denote the experimentally observed profiles.

(b) C_6H_6 flame (simulated profiles only).

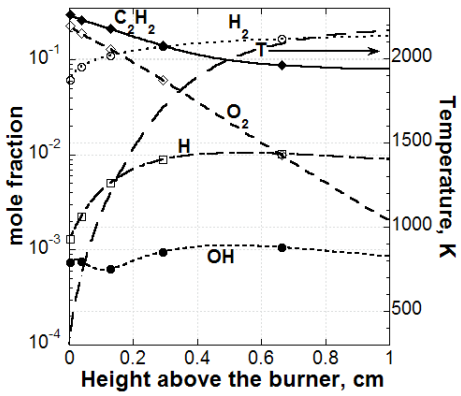

(c) C_2H_2 flame (simulated profiles only).

Figure 6: *Major chemical species profiles for the flames 1, 2 and 4, respectively (table 3).*

on C-H diagrams for the two flames. For the simulations using the KMC-ARS model, a seed molecule (or starting structure) is required. To study its effect on simulation results, computed C-H diagrams for flame 2 were obtained with two different seed molecules: pyrene and benzene (not shown here). No significant variation in the C-H diagrams with the seed molecule was obtained. In this work, pyrene was chosen as the seed molecule, as it is considered to be important for soot nucleation [3]. Figure 7 shows C-H diagrams for flame 2 at three different HABs. The dotted lines in the figures represent the positions of peri-condensed PAHs on C-H diagrams [39]. This has been provided as a guideline to observe the development of PAH ensembles with HAB. The data points above this line represent H–rich PAHs and below H–poor PAHs with respect to the most peri-condensed six-member ring structures [39]. The C-H diagrams show that the observed PAH ensembles at the three HABs were very well predicted by the KMC-ARS model. In this flame environment, benzene addition on PAHs was found to dominate over other reactions for the lower HABs (less than 7 mm), and the reactions involving acetylene dominated at

higher HABs. This result is in agreement with the prediction of [59]. Figure 8 shows a C-H diagram for flame 4 containing the simulated along with the experimentally observed ensemble of PAHs with upto 70 carbon atoms. It is evident from the C-H diagrams of the two flames that the concentration of data points near the peri-condensed line in case of flame 4 is higher than that of flame 2 indicating the presence of H-poorer PAHs in flame 4 as compared to PAHs in flame 2 with same C atom count. It was interesting to note that in both the flame environments, free-edge growth through route 2 (figure 3) dominated at lower flame temperatures (< 1000 K), and route 1 dominated at higher temperatures (or higher HABs). Figures 9(a) and 9(b) show computed PAHs from the two flames having the same number of C atoms. It is well known that the PAHs having 5-member rings bordered by not more than two 6-member rings are planar in geometry (the term "planar" refers to the planar arrangement of C atoms) [33]. PAHs with upto 70 C atoms from flame 5 mostly have 5-member rings on zig-zags, thus bordered by two six-member rings only, and a very few embedded 5-member rings. Hence, the simulation predicts almost planar PAHs for the C_2H_2 flame, as was observed in [64]. The embedded five-member rings occur due to the closure of 5-member bays with the present reaction mechanism. Bay sites on PAHs were observed to occur most commonly due to benzene addition reaction at lower HABs and due to free-edge growth reaction at higher HABs, and hence, bay closure reaction was more important in the environment of flame 2. Embedded 5-member rings formed due to closure of 5-member bays were common in computed PAHs from flame 2. Therefore, the simulation predicts PAHs with some geometrical distortions for this flame.

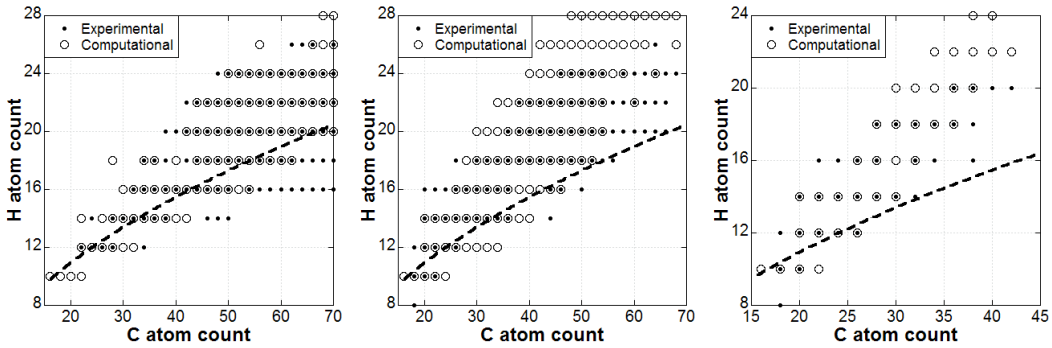

(a) HAB = 10 mm. (b) HAB = 7 mm. (c) HAB = 5 mm.

Figure 7: *C-H diagrams for the* C_6H_6 *flame at different HABs.*

The C-H diagrams presented in this paper contain data points corresponding to PAHs with even number of C and H atoms. PAHs with odd number of C atoms can arise due to: presence of aliphatics with odd number of C atoms like C_1 and C_3 hydrocarbons, presence of 5-member rings on free-edges (for example, indene) or on armchairs (for example fluorene), and presence of 6-member rings on zigzags (for example, phenalene). Reactions leading to PAHs with odd number of C atoms were not included in the reaction mechanism, and therefore, such PAHs were not obtained. These reactions will be explored in future studies.

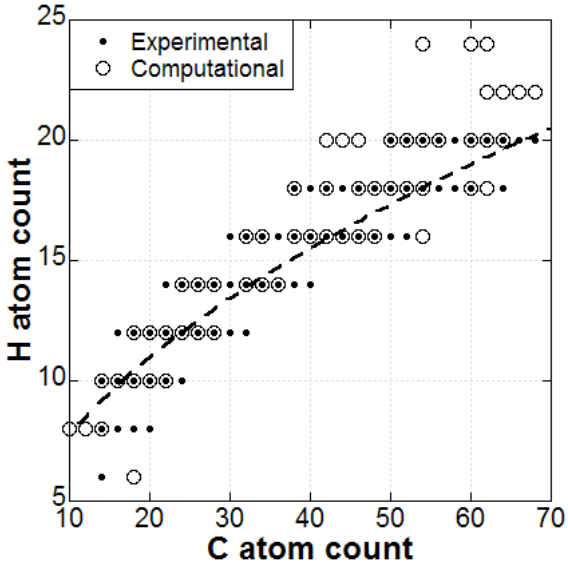

Figure 8: *C-H diagram for the* C_2H_2 *flame.*

The H content of PAHs with the same number of C atoms not only varies with the type of the fuel generating them, but also with HAB. The C-H diagrams for flame 2 in figure 7 show that PAHs at lower HABs are H-richer than those at higher HABs. It was suggested by Weilmünster et al. [64] that for the same number of C atoms, H-rich PAHs involve more bays and armchairs and less 5-member rings than H-poor PAHs. To verify this, ensembles of PAHs with the same number of C atoms were generated for different HABs, and the variation in the concentration of elementary sites on the PAHs with HAB was studied. Figure 10 shows the concentration of elementary sites on PAHs, represented in terms of their number fractions for different HABs and C atom counts. For the computed PAHs with n number of C atoms, the empirical mean of the number fraction of a site $S \in \{R5, ED, ZZ, AC, BY\}$, $x_{S,n}$ was obtained using the following expression:

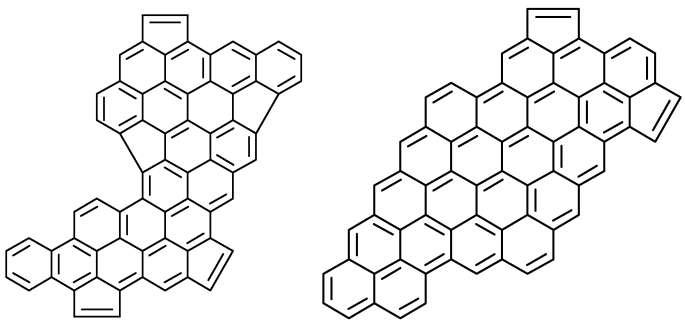

(a) C_6H_6 flame. (b) C_2H_2 flame.

Figure 9: *Example computed PAHs for the flames 2 and 4, respectively.*

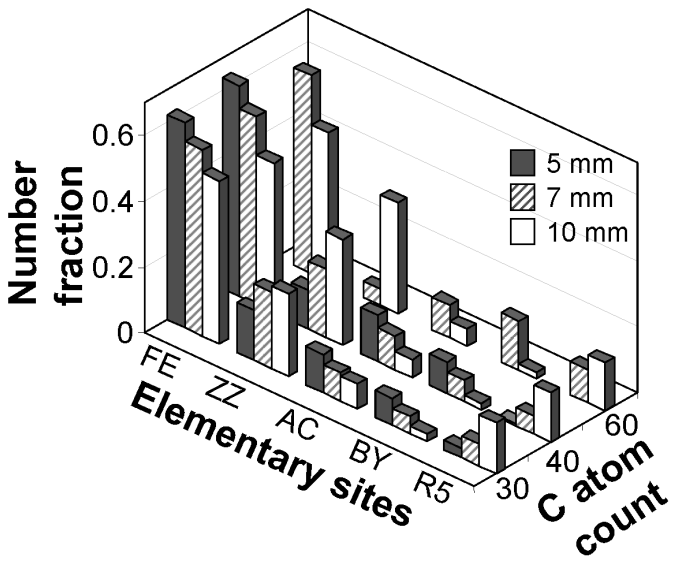

Figure 10: *Number fraction of elementary sites for different C atom counts and HABs.*

$x_{S,n} = \overline{N}_{S,n} / \sum_{i \in S} \overline{N}_{i,n}$, where $\overline{N}_{S,n}$ is the average number of sites of type S present on the PAHs. It is clear from figure 10 that for the PAHs with same number of C atoms, the number fractions of armchairs and bay sites decrease and that of 5-member rings increases with HAB, thus making PAHs H-poorer with HAB. This result is in line with the predictions of Weilmünster et al. [64].

The comparison of the computed results with experimental findings presented here suggests that the model is capable of predicting the experimental observations very well. However it is limited by the assumption of 2D growth of PAHs, and therefore, needs further improvement in the future.

6 Results and Discussion

The validation of the KMC-ARS model against some key experimental findings in the previous section warrants its use to get the statistical closure expressions for the site-counting model, as indicated in section 4. In order to obtain this closure, a detailed statistical analysis of the results based on the study of growth of PAHs in the flame environments listed in table 3 is presented.

6.1 Statistical Analysis

This section details the methodology adopted to obtain the unclosed terms in the site-counting model: N_y (correlations for combined sites) and $P_{S,m}$ (probabilities of elementary sites to act as neighbour sites in different processes). Additionally, the effect of steric hinderance in larger PAH structures is investigated. For the results presented in this sec-

tion, PAH growth simulations were carried out a large number of times in order to obtain average variations in the required random variables and confidence intervals over them (see section 3.5 for details).

6.1.1 Combined-Site Correlations

The site-counting model requires some approximations to describe the combined sites because it does not store the PAH structural information. Figure 11 shows four types of combined sites on an example PAH structure. The KMC-ARS model can be used to

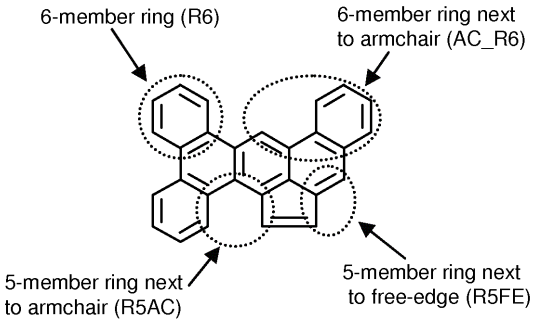

Figure 11: *An example PAH molecule showing combined sites.*

provide this information by developing correlations. The particle state space is multidimensional, therefore the number of combined sites will be functions of many variables, particularly the number of carbon atoms, and the number of all elementary sites. However, it was assumed to be sufficient to describe the combined site counts by just one particle property. The correlations for the combined sites are based on the variation in their counts with one of their constituent elementary sites. To obtain the correlations, the simulations described above were run 500 times and the combined site counts were stored along with the elementary site counts. Figure 12(a) shows the number of R6 rings as a function of free-edge count, and figure 12(b) shows the number of R6 rings adjacent to armchairs as a function of armchair count for flame 8. A nearly linear relationship was observed in all cases. The correlations were obtained by using a least-squares algorithm to fit a linear function to the data, averaged over all simulations. The correlations for the combined site, R5ZZ involved in process S14 (table 2) were not obtained as this reaction does not affect the site counts in the site-counting model [9]. Meaningful correlations for the combined site involving two FE's next to an embedded R5 (process S17, table 2) could not be obtained as it occurred very infrequently on the computed PAHs.

As an R6 ring consists of three consecutive free-edges, they cannot exist when there are just two free-edges, hence a correlation of the form $N_{R6} = a(N_{FE} - 2)$ was obtained. The armchair count was chosen as the fitting variable for the AC_R6 site count as the armchair count was always found to be lower than the free-edge count, hence the combined site count should be more sensitive to the number of armchairs. For the combined sites involving R5, the R5 count was chosen for the same reason. The correlations for the combined sites required by the site-counting model (N_y) were evaluated for all the flames

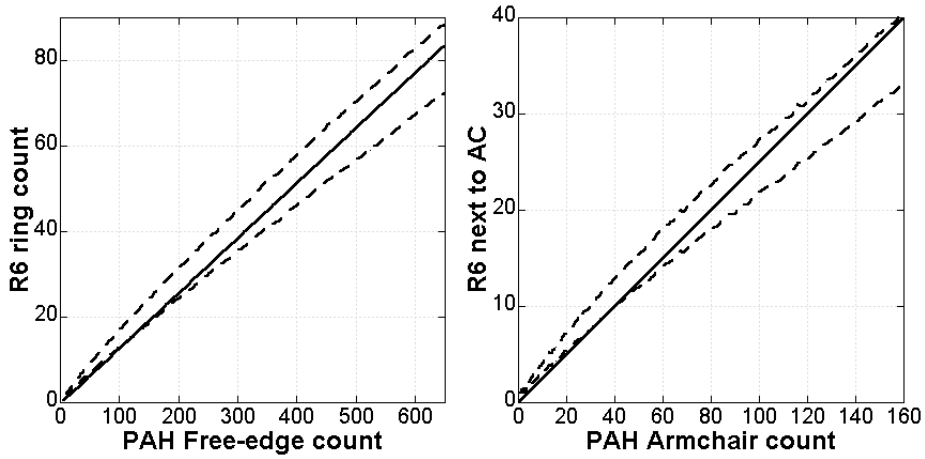

(a) R6 ring count as a function of free-edge count.

(b) AC.R6 site count (R6 ring next to an armchair) as a function of armchair count.

Figure 12: *Correlations for combined sites. Solid lines show linear approximations, dashed lines show confidence intervals.*

listed in table 3 to study their variation with flame properties like fuel, cold gas velocity, pressure and C/O ratio. In this paper, detailed statistics are provided only for atmospheric pressure flames 8–11. It is because such correlations have been used in [10] in the site counting model to predict the soot observables like soot volume fraction, number density and particle size distribution functions for flames 8–11. Given below are the correlations

for these flames:

$$N_{R6} = \begin{cases} 0.169 \times (N_{FE} - 2) & \text{if } N_{FE} > 2 \ \ (flame\ 8) \\ 0.168 \times (N_{FE} - 2) & \text{if } N_{FE} > 2 \ \ (flame\ 9) \\ 0.169 \times (N_{FE} - 2) & \text{if } N_{FE} > 2 \ \ (flame\ 10) \\ 0.166 \times (N_{FE} - 2) & \text{if } N_{FE} > 2 \ \ (flame\ 11) \\ 0 & \text{if } N_{FE} \leq 2 \end{cases} \tag{10}$$

$$N_{AC\_R6} = \begin{cases} 0.36 \times N_{AC} & \text{if } N_{FE} > 2,\ N_{AC} > 0 \ \ (flame\ 8) \\ 0.36 \times N_{AC} & \text{if } N_{FE} > 2,\ N_{AC} > 0 \ \ (flame\ 9) \\ 0.35 \times N_{AC} & \text{if } N_{FE} > 2,\ N_{AC} > 0 \ \ (flame\ 10) \\ 0.35 \times N_{AC} & \text{if } N_{FE} > 2,\ N_{AC} > 0 \ \ (flame\ 11) \\ 0 & \text{if } N_{FE} \leq 2,\ N_{AC} \leq 0 \end{cases} \tag{11}$$

$$N_{R5FE} = \begin{cases} 1.3 \times N_{R5} & \text{if } N_{FE} > 0,\ N_{R5} > 0 \ \ (flame\ 8) \\ 1.25 \times N_{R5} & \text{if } N_{FE} > 0,\ N_{R5} > 0 \ \ (flame\ 9) \\ 1.2 \times N_{R5} & \text{if } N_{FE} > 0,\ N_{R5} > 0 \ \ (flame\ 10) \\ 1.22 \times N_{R5} & \text{if } N_{FE} > 0,\ N_{R5} > 0 \ \ (flame\ 11) \\ 0 & \text{if } N_{FE} \leq 0,\ N_{R5} \leq 0 \end{cases} \tag{12}$$

$$N_{R5AC} = \begin{cases} 0.066 \times N_{R5} & \text{if } N_{AC} > 0,\ N_{R5} > 0 \ \ (flame\ 8) \\ 0.024 \times N_{R5} & \text{if } N_{AC} > 0,\ N_{R5} > 0 \ \ (flame\ 9) \\ 0.031 \times N_{R5} & \text{if } N_{AC} > 0,\ N_{R5} > 0 \ \ (flame\ 10) \\ 0.025 \times N_{R5} & \text{if } N_{AC} > 0,\ N_{R5} > 0 \ \ (flame\ 11) \\ 0 & \text{if } N_{AC} \leq 0,\ N_{R5} \leq 0 \end{cases} \tag{13}$$

It can be noticed that these correlations do not vary much for flames 8–11, and can be concluded that the change in cold gas velocity does not affect the correlations. In a similar fashion, correlations for flames 3–6 were evaluated. These low–pressure flames differed in C/O ratio and/or cold gas velocity. For these flames as well, correlations were found to be varying negligibly indicating no effect of C/O ratio on the correlations. Average values of the correlation coefficients for these flames along with the other flames simulated in this work are provided in table 4. It can be seen in table 4 that the correlations for the flames having different fuels but same pressure (flames 2–7) differ from each other. Similarly, comparing the correlations for flame 1 and flames 8–11 in the same table shows that the correlations are dependent on flame operating pressure as well. Since the correlations reflect the resulting PAH structure in a flame environment, the changes in correlations with the type of fuel and pressure of the flames may be due to the change in the dominant PAH growth processes (discussed in section 5 for C_6H_6 and C_2H_2 flames), which can significantly change the PAH structures [22]. The domination of a PAH growth process in a flame environment depends on its rate, which in turn depends on species concentration and rate constants of the PAH reactions (equation 4). Chemical species profiles vary significantly with the type of fuel in the flame (see figure 6), and the rate constants of PAH reactions depend on pressure [63]. Therefore, the dominant PAH processes in flames with varying pressure and/or fuels may be different, leading to a change in PAH structures and thus the correlations. The correlations and the PAH statistics discussed further in this

Table 4: *Correlation coefficients for the simulated flames.*

Flame	Correlation coefficients							
	$R6$[a]	AC_R6[b]	$R5FE$[c]	$R5AC$[d]	$unavail'FE$[e]		$unavail'AC$[f]	
	a	b	c	d	e_1	e_1	f_1	f_2
1	0.052	0.250	1.064	0.006	0.476	0.446	0.579	0.0.142
2	0.062	0.163	0.774	0.028	0.38	0.39	0.972	0.985
3–6	0.040	0.123	0.718	0.022	0.183	0.026	0.155	0.631
7	0.074	0.206	0.786	0.018	0.41	0.58	0.99	0.079
8–11	0.168	0.355	1.243	0.036	0.573	0.024	0.599	0.044

[a] $N_{R6} = a \times (N_{FE} - 2)$
[b] $N_{AC\_R6} = b \times N_{AC}$
[c] $N_{R5FE} = c \times N_{R5}$
[d] $N_{R5AC} = d \times N_{R5}$
[e] $N_{unavail'FE} = \tanh(e_1 \times \log(e_2 \times N_{FE} + 1))$
[f] $N_{unavail'AC} = \tanh(f_1 \times \log(f_2 \times N_{AC} + 1))$

paper have been provided for all the flames listed in table 3. This is to make the simulation of these flames along with the flames observed under similar conditions possible using the site-counting model to predict substantial details of soot particles like soot volume fraction, number density, particle size distribution functions, C/H ratio and average PAH sizes [9, 10].

6.1.2 Neighbour Statistics

When a surface reaction occurs it is necessary to update the neighbour site types, however, information about the neighbour sites is not available in the site-counting model. As outlined in section 4, $P_{S,m}$ is required to obtain this information. Only the jump processes involving six-member rings, and oxidation of reactive sites in table 2 are considered here, as those involving only 5-member rings do not change neighbour sites, and processes S7 and S8 were observed to occur so infrequently that meaningful statistics could not be obtained. It was initially assumed that neighbour sites of type $S \in \{ED, ZZ, AC, BY\}$ are selected for process m with the probability $P_{S,m}(t) = N_S(t)/N_{tot}(t)$, where $N_S(t)$ is the number of sites of type S at time t, $N_{tot}(t)$ is the total number of sites (ignoring 5-member rings), and $m \in \{1, \ldots, \text{number of processes in table 5}\}$ is the process index. However, it was found that when using these probabilities the site-counting model did not agree with the KMC-ARS model, which suggests that some sites are more likely than others to be neighbours for certain processes. Therefore, site count weights were introduced for each process such that the weighted counts are given by: $N'_{S,m}(t) = W_{S,m} \times N_S(t)$, hence the probability of a site of type S being selected at time t for process m becomes:

$$P_{S,m}(t) = \frac{N'_{S,m}(t)}{N'_{tot,m}(t)} \tag{14}$$

where $N'_{tot,m}(t)$ is the sum of the weighted site counts and depends on the process m. It is assumed that the site weights do not depend strongly on PAH size, therefore they are considered to be constant for each process. This assumption is supported by the KMC-ARS simulations conducted for this study.

In order to calculate the site-weights, several KMC-ARS simulations were performed. For each simulation there are K events, and K_m denotes the number of times event m occurred. On selection of the tth jump process, where $t \in \{1, 2, \ldots, K\}$, the following information was stored: the time point t, the jump process index, m_t, the types of both neighbour sites, $T_1(t)$ and $T_2(t)$ and the counts of all site types; $N_{ED}(t)$, $N_{ZZ}(t)$, $N_{AC}(t)$, $N_{BY}(t)$. $L_{S,m}$ shall denote the number of times a site of type S acted as a neighbour for process m. In the limit of large K_m, the probability of a site acting as a neighbour is assumed to approach $P_{S,m} = L_{S,m}/K_m$, therefore, by summing over each jump process and solving the following equation, the site-weights can be obtained:

$$\sum_{t=1}^{K_m} \frac{W_{S,m} N_S(t)}{W_{FE,m} N_{FE}(t) + W_{ZZ,m} N_{ZZ}(t) + W_{AC,m} N_{AC}(t) + W_{BY,m} N_{BY}(t)} = L_{S,m} \quad (15)$$

where $S \in \{ED, ZZ, AC, BY\}$ and $m \in \{1, \ldots, 9\}$ (processes listed in table 5). As there are four possible site types which may act as neighbours; free-edges (FE), zig-zags (ZZ), armchairs (AC) and bays (BY), equation 15 gives a system of four linear equations for each process m, which can be solved using a standard numerical technique such as a Newton method. Equation 15 was solved for the four elementary sites, with the additional constraints of $W_{S,m} \geq 0$ and $\sum_S W_{S,m} = 1$. Table 5 shows the site-weights for the principal reactions for flames 8–11. These weights are used to calculate $P_{S,m} = f\left(W_{S,m}\right)$ in the site-counting model using equation 14.

It is clear from table 5 that assuming equal weights for all the sites would lead to an unrealistic PAH molecule using the site-counting model. For the reactions involving R6 desorption and conversion of a 6-member ring to a 5-member ring, the free-edge site-weight ($W_{FE}(3-6)$) is zero, as it is not possible to desorb a six-member ring having more than three consecutive free-edges together with the current reaction mechanism. Thus, a free-edge cannot exist as the neighbour site of a R6 ring. Similarly, for armchair oxidation reactions (reactions S11 and S12 in table 2), a free-edge cannot exist as a neighbour site. Therefore, the free-edge site-weight ($W_{FE}(7,8)$) is zero. For a 6-member bay closure reaction, a bay cannot be present as a neighbour, as it is geometrically prohibited. Therefore, for this reaction, W_{BY} is zero. A study on the variation in neighbour site-weights with flame properties was also conducted. It can be seen in table 5 that these weights for flames 8–11 do not vary significantly indicating no effect of cold gas velocity on them. Variation in the neighbour site-weights with $\mathrm{C/O}$ ratio, operating pressure and type of fuel of the flames has been shown graphically in figures 13, 14 and 15 respectively. It can be easily concluded from these figures that the site-weights do not vary significantly with $\mathrm{C/O}$ ratio (variation within 8%), but varies with the type of fuel and pressure, as was observed in the case of combined sites correlations.

Table 5: *Neighbour site-weights for the principal reactions for flames 8–11*

No.	Process	Reaction	Flame	W_{FE}	W_{ZZ}	W_{AC}	W_{BY}
1	S1	FE growth	C1	0.24	0.24	0.3	0.22
			C2	0.23	0.26	0.31	0.2
			C3	0.22	0.26	0.31	0.21
			C4	0.22	0.26	0.31	0.21
2	S2	AC growth	C1	0.38	0.26	0.19	0.17
			C2	0.38	0.27	0.19	0.16
			C3	0.38	0.28	0.19	0.15
			C4	0.38	0.27	0.19	0.16
3	S3	R6 desorption	C1	0	0.19	0.38	0.43
			C2	0	0.21	0.37	0.43
			C3	0	0.21	0.37	0.42
			C4	0	0.21	0.36	0.43
4	S4	R6 to R5 at AC	C1	0	0.19	0.39	0.42
			C2	0	0.2	0.37	0.43
			C3	0	0.23	0.39	0.38
			C4	0	0.20	0.36	0.44
5	S9	FE oxidation by O_2	C1	0	0.19	0.37	0.44
			C2	0	0.21	0.37	0.43
			C3	0	0.21	0.36	0.43
			C4	0	0.21	0.39	0.4
6	S10	FE oxidation by OH	C1	0	0.19	0.37	0.44
			C2	0	0.21	0.37	0.43
			C3	0	0.21	0.36	0.43
			C4	0	0.21	0.39	0.4
7	S11	AC oxidation by O_2	C1	0	0.37	0.4	0.23
			C2	0	0.35	0.36	0.29
			C3	0	0.35	0.36	0.29
			C4	0	0.37	0.37	0.26
8	S12	AC oxidation by OH	C1	0	0.37	0.4	0.23
			C2	0	0.35	0.36	0.29
			C3	0	0.35	0.36	0.29
			C4	0	0.37	0.37	0.26
9	S15	Bay closure	C1	0.41	0.29	0.30	0
			C2	0.41	0.29	0.30	0
			C3	0.42	0.29	0.29	0
			C4	0.43	0.29	0.28	0

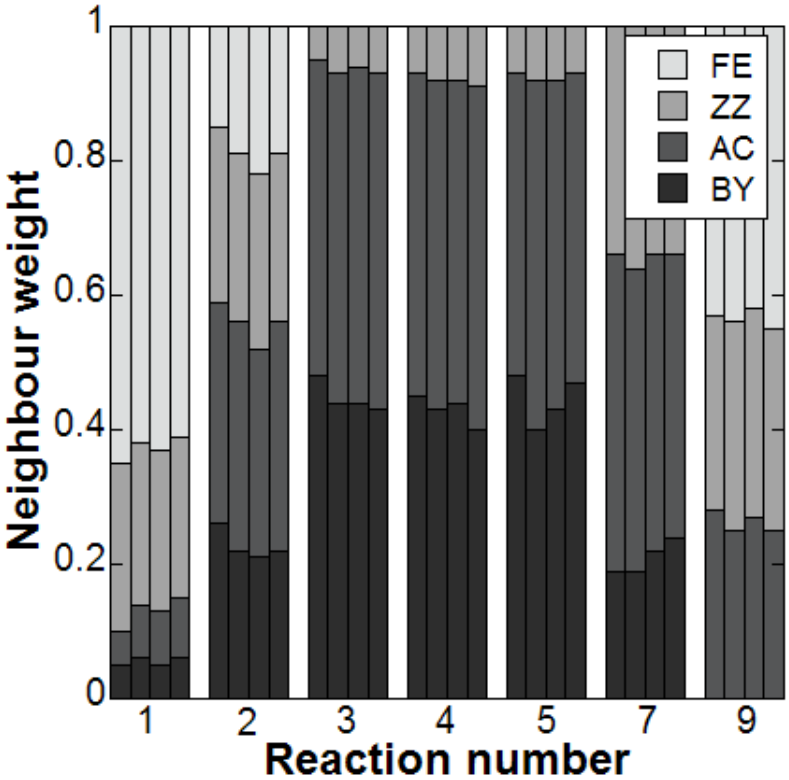

Figure 13: *Neighbour site-weights of elementary sites for different reactions for the* C_2H_2 *flames(flames 3–6). The reactions corresponding to the reaction numbers (on x-axis) are listed in table 5. For each reaction, the four consecutive parallel stacks represent flames 3 to 6 from left to right.*

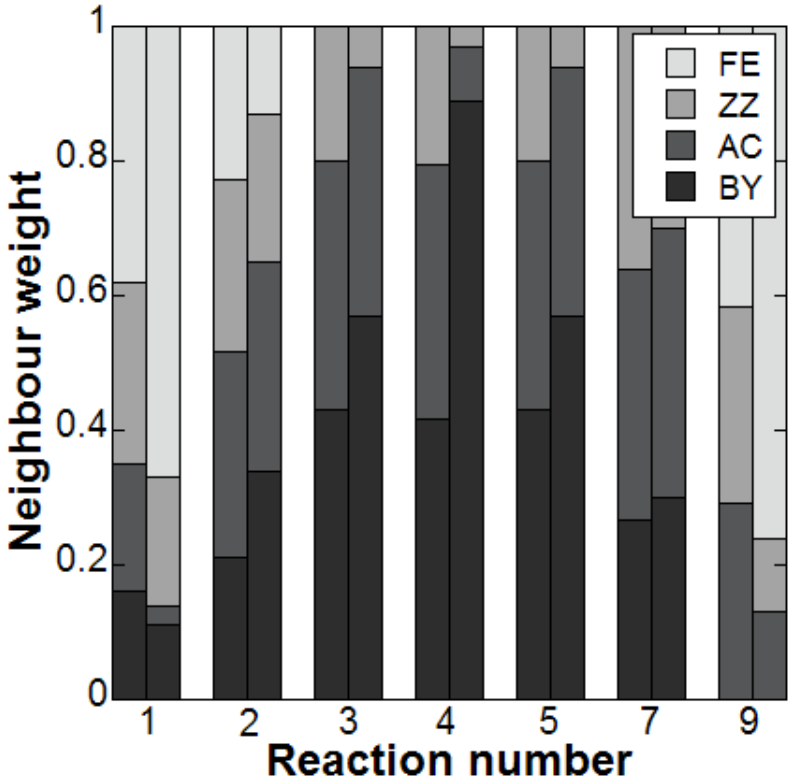

Figure 14: *Variation in neighbour site-weights of elementary sites for different reactions with pressure for the* C_2H_4 *flame. The reactions corresponding to the reaction numbers (on x-axis) are listed in table 5. For each reaction, first stack represents average neighbour site-weights for flames 8–11, and second stack represents flame 1.*

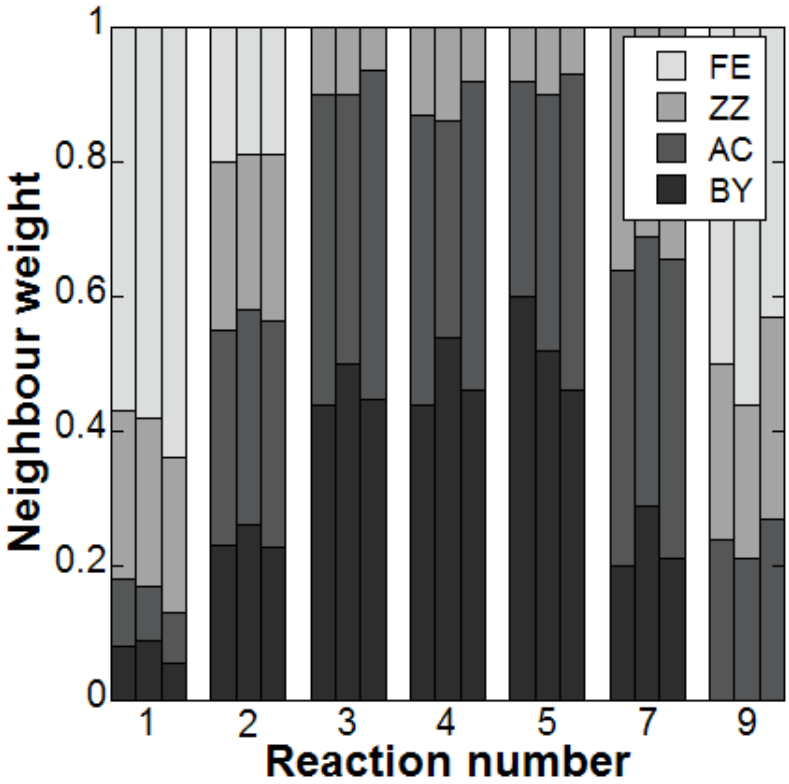

Figure 15: *Variation in neighbour site-weights of elementary sites for different reactions with the type of fuel. The reactions corresponding to the reaction numbers (on x-axis) are listed in table 5. For each reaction, the three consecutive parallel stacks represent three different flames at the same pressure (2.67 kPa): first stack–*C_6H_6 *flame (flame 2), second stack–*C_2H_4 *flame (flame 7), third stack–*C_2H_2 *flame (flames 3–6).*

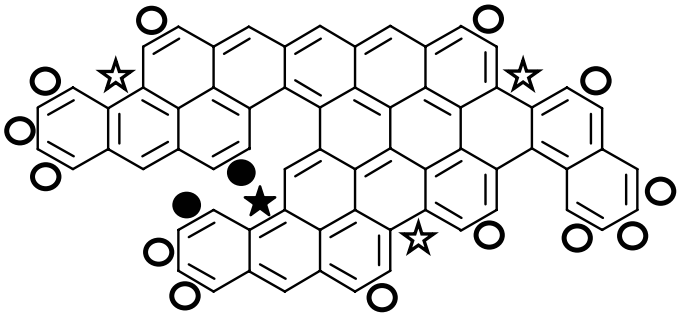

Figure 16: *A computed PAH molecule from flame 8 at HAB = 5 mm. Filled circles and stars denote unavailable free-edges and armchairs respectively. Hollow symbols denote available sites.*

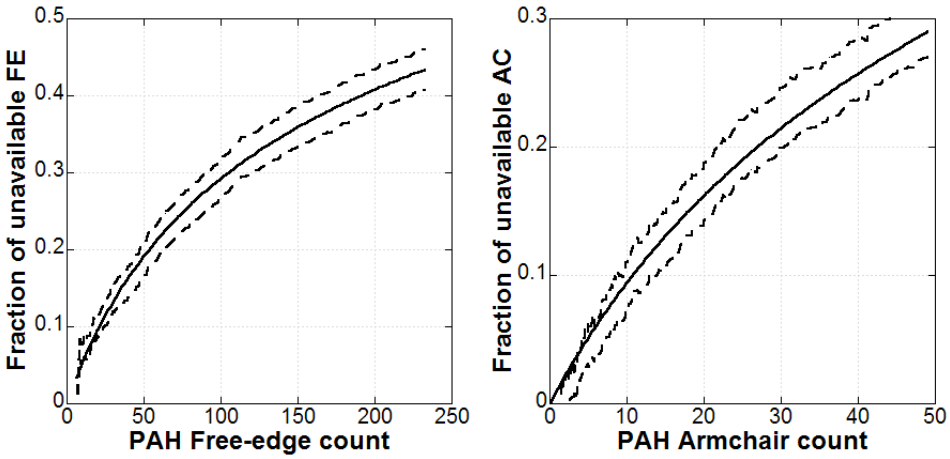

(a) Fraction of unavailable free-edges. (b) Fraction of unavailable armchairs.

Figure 17: *Unavailable sites. Solid lines show a* tanh *fit. Dashed lines show confidence intervals.*

6.1.3 Unavailable Sites

As PAH molecules grow, their structure can become complex and it is possible for some sites to be unavailable for reaction because they are hindered by nearby aromatic rings. This has been referred to as steric hinderance. Figure 16 shows how free-edges and armchairs can become unavailable on a computed PAH molecule from flame 8. This generally occurs when the structure grows around on itself. This effect should also be observed if PAH molecules are stacked close together, and is probably one of the major contributing factors of the alpha correlation for inactive sites in the ABF model [3]. Such contorted structures, as observed in figure 16 would most likely give rise to a 3D structure as the nearby hydrogen atoms interact, however, if the molecule was constrained in a stack this may be less energetically favourable. It is more likely in this case that the hydrogen are abstracted and a C-C bond is formed through bay closure reactions later on in the flame.

The KMC-ARS model allows unavailable sites to be counted explicitly. Figures 17(a) and 17(b) show the fraction of unavailable free-edges and armchairs respectively as functions of the free-edge and armchair counts. The fraction of unavailable sites firstly increases with the site counts before reaching an asymptotic limit at larger site counts. A function of the form $Y = \tanh(a \times \log(bX + 1))$ was found to describe this asymptotic behaviour well. The curves in figure 17 were fitted by trial and error, and the equations for flames 8–11 are given below:

$$N_{unavail'FE} = \begin{cases} \tanh(0.573 \times \log(0.024 \times N_{FE} + 1) & flame\ 8 \\ \tanh(0.752 \times \log(0.018 \times N_{FE} + 1) & flame\ 9 \\ \tanh(0.852 \times \log(0.016 \times N_{FE} + 1) & flame\ 10 \\ \tanh(0.984 \times \log(0.014 \times N_{FE} + 1) & flame\ 11 \end{cases} \tag{16}$$

$$N_{unavail'AC} = \begin{cases} \tanh(0.599 \times \log(0.044 \times N_{AC} + 1) & flame\ 8 \\ \tanh(0.777 \times \log(0.037 \times N_{AC} + 1) & flame\ 9 \\ \tanh(0.867 \times \log(0.031 \times N_{AC} + 1) & flame\ 10 \\ \tanh(0.934 \times \log(0.024 \times N_{AC} + 1) & flame\ 11 \end{cases} \tag{17}$$

The above equations predict very similar variation of unavailable free-edges with free-edges count for flames 8–11. The equations for unavailable armchairs show a similar trend. Therefore, the correlation coefficient for only flame 8 is presented in table 4. A similar trend was observed for flames 4–7. Therefore correlation coefficients for only flame 4 is provided in the same table along with the coefficients for other flames listed in table 3. The equations of the above form are remarkably similar to the alpha correlation [3], used in the ABF soot model to determine empirically the number of active sites on soot particles. The alpha correlation is used to model particle "aging", which is the observed phenomenon that soot particle become less reactive with age. The correlations presented here have a similar role, as they effectively decrease the number of active sites present on the PAHs with the simulation time.

6.2 Site-Counting Model Validation

The statistics and correlations described above were implemented in the site-counting model, and identical simulations were performed using the site-counting model and the KMC-ARS model for flame 11. Figure 18 shows the comparison of the PAH characteristics: carbon atom count and number of elementary sites on the PAHs in flame 11.

Figure 18(a) shows that the site-counting model and the KMC-ARS model predict similar carbon atom counts at all observed flow times. Figure 18(b) shows that the agreement for the number of free-edges, zig-zags and armchairs is reasonable also. The close agreement of the number of elementary sites is important because the site counts are used to calculate the process rates. Also, this signifies that the site-counting model predicts PAHs very similar to those computed by the KMC-ARS model. The site-counting model has also been validated in our previous work [9] in a flame-like environment. The extent of

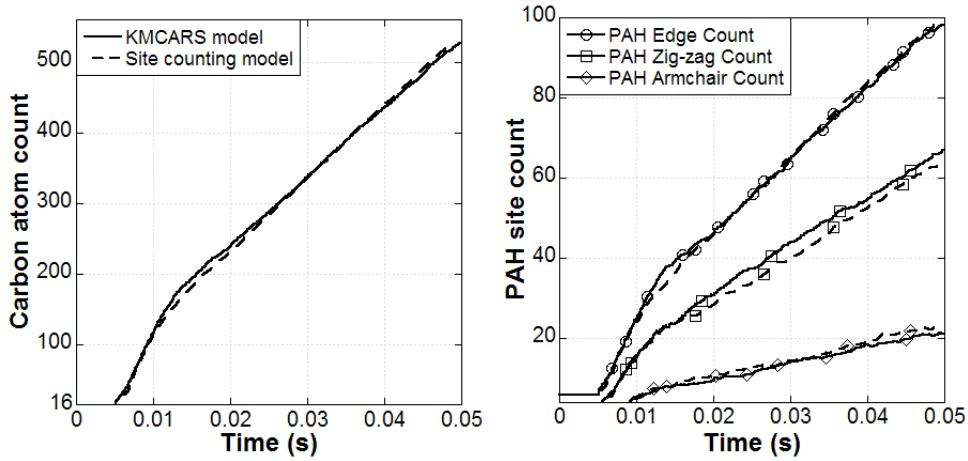

(a) C atom count as a function of time

(b) Site count as a function of time

Figure 18: *Comparison of the results from the KMC-ARS model and the site-counting model for flame 11. Dashed lines show the results from the site-counting model and solid lines show the result from the KMC-ARS model.*

agreement of the computed PAH characteristics by the two models is very encouraging. It shows that the detailed PAH growth model can be confidently accommodated into a soot particle population balance using the site-counting model.

As the PAH molecules present in flames are very small in size (PAHs with less than 100 C atoms are observed in flames [12, 56]), a comparison between the two models was carried out over this range with and without the correlation for unavailable sites, to test its importance in the experimental size range. Figure 19 shows the variation in the number of PAH sites with the number of C atoms for this case. It can be concluded from this figure that the correlations for unavailable sites are not very significant for small PAH molecules.

7 Conclusion

A new detailed PAH growth model (KMC-ARS model) has been developed. This model considers growth of a PAH molecule in all directions, irrespective of the orientation of reactive sites. A large set of PAH processes along with the reactions involved in the PAH growth has been presented. DFT simulations to evaluate the rates of the reactions involved in the cyclodehydrogenation process to form a 6-member ring on PAHs have been carried out. An algorithm has been developed to track the structure of a PAH molecule, as it grows in a flame-like environment. This model allows the exact estimation of the distribution of sites on a PAH molecule. However, the computational time required to track the growth of a single PAH molecule is very high, therefore it is computationally unfeasible to incorporate this detailed PAH growth model into a soot particle population balance.

The site-counting model proposed by Celnik et al. [9] allows this detailed PAH growth

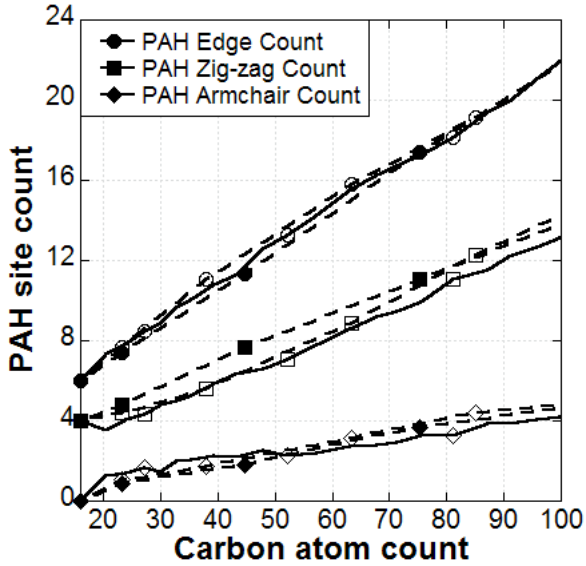

Figure 19: *Comparison of the results: Dashed lines show the results from the site-counting model and solid lines from the KMC-ARS model. Filled symbols show the results from site-counting model without correlations for unavailable sites.*

model to be coupled into soot particle population balances by neglecting PAH structure. This model is computationally very fast (computational time required to track the growth of a single PAH molecule is about 1.5 seconds with the site-counting model, and is about 30 minutes with the KMC-ARS model for a KMC simulation of 2.4 ms). Since the site-counting model neglects the PAH structure, the structural information about the PAH molecule is provided by the KMC-ARS model. Correlations have been developed for different flame environments which describe the number of combined sites (more than one adjacent site), which are required to calculate the rates of some reactions. Site type weights have been found which allow neighbour sites to be selected appropriately without prior knowledge of the structure. A method to calculate the site weights using results obtained using the KMC-ARS model has been described.

It has also been shown that as a PAH molecule grows, reactive sites can become unavailable due to steric hindrance. The fraction of unavailable sites increases rapidly with the size of the PAHs initially, but shows an asymptotic behaviour afterwards. Correlations for the fraction of unavailable sites have also been developed. All the PAH statistics detailed in this paper have been shown to be independent of cold gas velocity and $\mathrm{C/O}$ ratio of the flames, but depend on the type of fuel and pressure. The statistics have been obtained for the commonly observed premixed laminar flames, which can be used in the site-counting model along with soot particle population balance to predict soot observables like soot volume fraction, number density, particle size distribution functions, C/H ratio and average PAH sizes [9, 10]. The results of the KMC-ARS model have been compared to the site-counting model. The agreement between the carbon atom counts and the principal site counts is reasonable, which suggests that the detailed PAH growth model can

be implemented in the soot particle population balances through the site-counting model without much loss of information.

Acknowledgement

A.R. is grateful to Cambridge Commonwealth Trusts (CCT) and Clare College, Cambridge for their financial support. The authors highly acknowledge the support of EPSRC under EP/C547241/1 and EP/E01724X/1.

References

[1] A. D. Abid, N. Heinz, E. D. Tolmachoff, D. J. Phares, and H. Wang. Relation between particle size distribution function and morphology of soot formed in atmospheric-pressure, premixed ethylene-oxygen-argon flame. In *5th US Combustion Meeting Papers*. Western States Section of the Combustion Institute, March 2007. Paper # F11.

[2] M. A. Allen, Y. L. Yung, and G. R. Gladstone. The relative abundance of ethane to acetylene in the jovian stratosphere. *Icarus*, 100:527–533, 1992. doi:10.1016/0019-1035(92)90115-N.

[3] J. Appel, H. Bockhorn, and M. Frenklach. Kinetic modeling of soot formation with detailed chemistry and physics: Laminar premixed flames of C_2 hydrocarbons. *Combust. Flame*, 121:122–136, 2000. doi:10.1016/S0010-2180(99)00135-2.

[4] M. Balthasar and M. Kraft. A stochastic approach to solve the particle size distribution function of soot particles in laminar premixed flames. *Combust. Flame*, 133: 289–298, 2003. doi:10.1016/S0010-2180(03)00003-8.

[5] A. Bhargava and P. R. Westmoreland. Measured Flame Structure and Kinetics in a Fuel-Rich Ethylene Flame. *Combust. Flame*, 113:333–347, 1998. doi:10.1016/S0010-2180(97)00208-3.

[6] A. D. Boese and N. C. Handy. *J. Chem. Phys.*, 114:5497, 2001.

[7] H. Böhm and H. Jander. PAH formation in acetylene-benzene pyrolysis. *Phys. Chem. Chem. Phys.*, 1:3775–3781, 1999.

[8] A. Braun, F. E. Huggins, N. Shah, Y. Chen, S. Wirick, S. B. Mun, C. Jacobsen, and G. P. Huffman. Advantages of soft X-ray absorption over TEM-EELS for solid carbon studies – a comparative study on diesel soot with EELS and NEXAFS. *Carbon*, 43:117–124, 2005. doi:10.1016/j.carbon.2004.08.029.

[9] M. S. Celnik, A. Raj, R. H. West, R. I. A. Patterson, and M. Kraft. An aromatic site description of soot particles. Technical Report 51, c4e Preprint-Series, Cambridge, 2007. URL `http://como.cheng.cam.ac.uk`. Material from this preprint has been published in [11].

[10] M. S. Celnik, M. Sander, A. Raj, R. H. West, and M. Kraft. Modelling soot formation in a premixed flame using an aromatic-site model and an improved oxidation rate. Technical Report 53, c4e Preprint-Series, Cambridge, 2007. URL `http://como.cheng.cam.ac.uk`.

[11] M. S. Celnik, A. Raj, R. H. West, R. I. A. Patterson, and M. Kraft. An aromatic site description of soot particles. *Combust. Flame*, 2008. doi:10.1016/j.combustflame.2008.04.011. . In press.

[12] H. X. Chen and R. A. Dobbins. Crystallogenesis of Particles Formed in Hydrocarbon Combustion. *Combust. Sci. Technol.*, 159, 2000.

[13] J. Cioslowski, G. Liu, and D. Moncrieff. Nonclassical Aryl Radicals: Intermediates or Transition States for the Hydrogen Shift Reactions? *J. Org. Chem.*, 61:4111–4114, 1996.

[14] J. Cioslowski, P. Piskorz, and D. Moncrieff. Thermally Induced Cyclodehydrogenation of Biaryls: A Simple Radical Reaction or a Sequence of Rearrangements? *J. Org. Chem.*, 63:4051–4054, 1998.

[15] A. D'Anna, A. Rolando, C. Allouis, P. Minutolo, and A. D'Alessio. Nano-organic carbon and soot particle measurements in a laminar ethylene diffusion flame. *Proc. Combust. Inst.*, 30:1449–1456, 2004. doi:10.1016/j.proci.2004.08.276.

[16] M. J. S. Dewar, W. C. G. Jr, M. Frenklach, and I. Oref. Rate Constant for Cyclization/Decyclization of the Phenyl Radical. *J. Am. Chem. Soc.*, 109:4456–4457, 1987. doi:10.1021/ja00249a005.

[17] S. di Stasio. Electron microscopic evidence of aggregation under three different size scales for soot nanoparticles in flame. *Carbon*, 39:109–118, 2001. doi:10.1016/S0008-6223(00)00099-3.

[18] A. Fahr and S. E. Stein. Reactions of vinyl and phenyl radicals with ethyne, ethene and benzene. *Proc. Combust. Inst.*, 22:1023–1029, 1989.

[19] M. Frenklach. On surface growth mechanism of soot particles. *Proc. Combust. Inst.*, 26:2285–2293, 1996. doi:10.1016/S0082-0784(96)80056-7.

[20] M. Frenklach. Method of moments with interpolative closure. *Chem. Eng. Sci*, 57: 2229–2239, 2002. doi:10.1016/S0009-2509(02)00113-6.

[21] M. Frenklach and E. D. Feigelson. Formation of polycyclic aromatic hydrocarbons in circumstellar envelopes. *Astrophys. J.*, 341:372–384, 1989.

[22] M. Frenklach and S. J. Harris. Aerosol dynamics modeling using the method of moments. *J. Colloid Interf. Sci.*, 118(1):252–261, 1987. doi:10.1016/0021-9797(87)90454-1.

[23] M. Frenklach and H. Wang. Detailed modeling of soot particle nucleation and growth. *Proc. Combust. Inst.*, 23:1559–1566, 1990. doi:10.1016/S0082-0784(06)80426-1.

[24] M. Frenklach and H. Wang. Detailed surface and gas-phase chemical kinetics of diamond deposition. *Phys. Rev. B*, 43(2):1520–1545, 1991. doi:10.1103/PhysRevB.43.1520.

[25] M. Frenklach and H. Wang. *Detailed Mechanism and Modelling of Soot Particle Formation*, volume 59 of *Series in Chemical Physics*, pages 162–190. Springer Verlag, Berlin, 1994. ISBN 354058398X 9783540583981.

[26] M. Frenklach, N. W. Moriarty, and N. J. Brown. Hydrogen migration in polyaromatic growth. *Proc. Combust. Inst.*, 27(2):1655–1661, 1998. doi:10.1016/S0082-0784(98)80004-0.

[27] M. Frenklach, C. A. Schuetz, and J. Ping. Migration mechanism of aromatic-edge growth. *Proc. Combust. Inst.*, 30:1389–1396, 2005. doi:10.1016/j.proci.2004.07.048.

[28] R. G. Gilbert, K. Luther, and J. Troe. *Ber. Bunsenges. Phys. Chem.*, 87:169, 1983.

[29] B. Gómez-Lor, C. Koper, R. H. Fokkens, E. J. Vlietstra, T. J. Cleij, L. W. Jenneskens, N. M. M. Nibbering, and A. M. Echavarren. Zipping up 'the crushed fullerene' $C_{60}H_{30}$: C_{60} by fifteen-fold consecutive intramolecular H_2 losses. *Chem. Comm.*, pages 370–371, 2002. doi:10.1039/b110587f.

[30] L. A. Gribov, I. A. Novakov, A. I. Pavlyuchko, and E. V. Vasilev. Spectroscopic calculations of ch bond dissociation energy in the series of chloro derivatives of methane, ethane and propane. *J. Struct. Chem+.*, 47:635–641, 2006.

[31] B. S. Haynes and H. G. Wagner. Soot formation. *Prog. Energy Combust. Sci.*, 7(4): 229–273, 1981. doi:10.1016/0360-1285(81)90001-0.

[32] K. H. Homann. Carbon formation in premixed flames. *Combust. Flame*, 11(4): 265–287, 1967. doi:10.1016/0010-2180(67)90017-X.

[33] K. H. Homann. Fullerenes and Soot Formation–New Pathways to Large Particles in Flames. *Angew. Chem.*, 37:2434–2451, 1998.

[34] T. Ishiguro, Y. Takatori, and K. Akihama. Microstructure of Diesel Soot Particles Probed by Electron Microscopy: First Observation of Inner Core and Outer Shell. *Combust. Flame*, 108:231–234, 1997. doi:10.1016/S0010-2180(96)00206-4.

[35] S. Izvekov, A. Violi, and G. A. Voth. Systematic course-graining of nanoparticle interactions in molecular dynamics simulation. *J. Phys. Chem. B.*, 109:17019–17024, 2005.

[36] A. Kazakov, H. Wang, and M. Frenklach. Detailed modeling of soot formation in laminar premixed ethylene flames at a pressure of 10 bar. *Combust. Flame*, 100: 111–120, 1995. doi:10.1016/0010-2180(94)00086-8.

[37] J. Kee, K. Grcar, M. D. Smooke, and J. A. Miller. PREMIX: A fortran program for modelling steady laminar one-dimensional premixed flames. Technical report, SANDIA National Laboratories, 1985.

[38] R. J. Kee, F. M. Ropley, E. Meeks, and J. A. Miller. CHEMKIN-III: A FORTRAN chemical kinetics package for the analysis of gas-phase chemicl and plasma kinetics. Technical Report UC-405 SAND96-8216, Sandia National Laboratories, Livermore, CA 94551-0969, USA, May 1996.

[39] A. Keller, R. Kovacs, and K. H. Homann. Large molecules, ions, radicals and small soot particles in fuel rich hydrocarbon flames. *Phys. Chem. Chem. Phys.*, 2, 2000.

[40] J. H. Kiefer, L. J. Mizerka, M. R. Patel, and H. C. Wei. A Shock Tube Investigation of Major Pathways in the High-Temperature Pyrolysis of Benzene. *J. Phys. Chem.*, 89:2013–2019, 1985. doi:10.1021/j100256a043.

[41] V. D. Knyazev, A. Bencsura, S. I. Stoliarov, and I. R. Slagle. Kinetics of the $C_2H_3 + H \rightleftharpoons H + C_2H_4$ and $CH_3 + H_2 \rightleftharpoons H + CH_4$ Reactions. *J. Phys. Chem.*, 100: 11346–11354, 1996. doi:10.1021/jp9606568.

[42] A. M. Mebel, M. C. Lin, T. Yu, and K. Morokuma. Theoretical Study of Potential Energy Surface and Thermal Rate Constants for the $C_6H_5 + H_2$ and $C_6H_6 + H$ Reactions. *J. Phys. Chem. A*, 101:3189–3196, 1997. doi:10.1021/jp9702356.

[43] A. M. Mebel, M. C. Lin, D. Chakraborty, J. Park, S. H. Lin, and Y. T. Lee. Ab initio molecular orbital/Rice-Ramsperger-Kassel-Marcus theory study of multichannel rate constants for the unimolecular decomposition of benzene and the $H + C_6H_5$ reaction over the ground electronic state. *J. Chem. Phys.*, 114(19):8421, 2001. doi:10.1063/1.1360201.

[44] J. Park, S. Burova, A. S. Rodgers, and M. C. Lin. Experimental and Theoretical Studies of the $C_6H_5 + C_6H_6$ Reaction. *J. Phys. Chem. A*, 103:9036–9041, 1999. doi:10.1021/jp9920592.

[45] S. H. Park, S. N. Rogak, W. K. Bushe, J. Z. Wen, and M. J. Thomson. An aerosol model to predict size and structure of soot particles. *Combust. Theor. Model.*, 9(3): 499–513, 2005. doi:10.1080/13647830500195005.

[46] R. I. A. Patterson and M. Kraft. Models for the aggregate structure of soot particles. *Combust. Flame*, 151:160–172, 2007. doi:10.1016/j.combustflame.2007.04.012.

[47] H. Richter and J. Howard. MIT combustion mechanism, 2004. URL `web.mit.edu/anish/www/MITcomb.html`.

[48] H. Richter, W. J. Grieco, and J. B. Howard. Formation mechanism of polycyclic aromatic hydrocarbons and fullerenes in premixed benzene flames. *Combust. Flame*, 119:1–22, 1999. doi:10.1016/S0010-2180(99)00032-2.

[49] H. Richter, S. Granata, W. H. Green, and J. B. Howard. Detailed modelling of PAH and soot formation in a laminar premixed benzene/oxygen/argon low-pressure flame. *Proc. Combust. Inst.*, 30:1397–1405, 2005. doi:10.1016/j.proci.2004.08.088.

[50] P. N. Romani. Recent Rate Constant and Product Measurements of the Reaction $C_2H_3 + H_2$ and $C_2H_3 + H$—Importance for Photochemical Modeling of Hydrocarbons on Jupiter. *Icarus*, 122:233–241, 1996. doi:10.1006/icar.1996.0122.

[51] J. Singh, R. I. A. Patterson, M. Kraft, and H. Wang. Numerical simulation and sensitivity analysis of detailed soot particle size distribution in laminar premixed ethylene flames. *Combust. Flame*, 145:117–127, 2006. doi:10.1016/j.combustflame.2005.11.003.

[52] G. P. Smith, D. M. Golden, M. Frenklach, N. W. Moriarty, B. Eiteneer, M. Goldenberg, C. T. Bowman, R. K. Hanson, S. Song, W. C. G. Jr., V. V. Lissianski, and Z. Qin. GRI–Mech 3.0. URL `http://www.me.berkeley.edu/gri-mech/`.

[53] W. Tsang and R. F. Hampson. Chemical Kinetic Data Base for Combustion Chemistry. Part I. Methane and Related Compounds. *J Phys. Chem. Ref. Data*, 15:1087, 1986.

[54] B. V. Unterreiner, M. Sierka, and R. Ahlrichs. Reaction pathways for growth of polycyclic aromatic hydrocarbons under combustion conditions, a DFT study. *Phys. Chem. Chem. Phys.*, 6:4377–4384, 2004. doi:10.1039/b407279k.

[55] R. L. Vander Wal. A TEM Methodology for the Study of Soot Particle Structure. *Combust. Sci. Tech.*, 126:333–357, 1997.

[56] R. L. Vander Wal. An Illustration of Soot Structure by Dark Field Transmission Electrom Microscopy. *Combust. Sci. Tech.*, 132, 1998.

[57] R. L. Vander Wal and A. J. Tomasek. Soot oxidation: dependence upon initial nanostructure. *Combust. Flame*, 134:1–9, 2002. doi:10.1016/S0010-2180(03)00084-1.

[58] R. L. Vander Wal, A. Yezerets, N. W. Currier, D. H. Kim, and C. M. Wang. HRTEM Study of diesel soot collected from diesel particulate filters. *Carbon*, 45:70–77, 2007. doi:10.1016/j.carbon.2006.08.005.

[59] A. Violi. Modeling of soot particle inception in aromatic and aliphatic premixed flames. *Combust. Flame*, 139:279–287, 2004. doi:10.1016/j.combustflame.2004.08.013.

[60] A. Violi. Cyclodehydrogenation Reactions to Cyclopentafused Polycyclic Aromatic Hydrocarbons. *J. Phys. Chem. A*, 109:7781–7787, 2005. doi:10.1021/jp052384r.

[61] A. Violi, G. A. Voth, and A. F. Sarofim. The relative roles of acetylene and aromatic precursors during particle inception. *Proc. Combust. Inst.*, 30:1343–1351, 2005. doi:10.1016/j.proci.2004.08.226.

[62] H. Wang and M. Frenklach. Calculations of rate coefficients for the chemically activated reactions of acetylene with vinylic and aromatic radicals. *J. Phys. Chem.*, 98(44):11465–11489, 1994. doi:10.1021/j100095a033.

[63] H. Wang and M. Frenklach. A detailed kinetic modeling study of aromatic formation in laminar premixed acetylene and ethylene flames. *Combust. Flame*, 110:173–221, 1997. doi:10.1016/S0010-2180(97)00068-0.

[64] P. Weilmünster, A. Keller, and K. H. Homann. Large Molecules, Radicals, Ions, and Small Soot Particles in Fuel-Rich Hydrocarbon Flames Part I: Positive Ions of Polycyclic Aromatic Hydorcarbons(PAH) in Low-Pressure Premixed Flames of Acetylene and Oxygen. *Combust. Flame*, 116:62–83, 1999. doi:10.1016/S0010-2180(98)00049-2.

[65] J. Z. Wen, M. J. Thomson, S. H. Park, S. N. Rogak, and M. F. Lightstone. Study of soot growth in a plug flow reactor using a moving sectional model. *Proc. Combust. Inst.*, 30(1):1477–1484, 2005. doi:10.1016/j.proci.2004.08.178.

[66] X. Xue and L. T. Scott. Thermal Cyclodehydrogenations To Form 6-Membered Rings: Cyclizations of [5]Helicenes. *Org. Lett.*, 9:3937–3940, 2007.

[67] B. Zhao, Z. Yang, M. V. Johnston, H. Wang, A. S. Wexler, M. Balthasar, and M. Kraft. Measurement and numerical simulation of soot particle size distribution functions in a laminar premixed ethylene-oxygen-argon flame. *Combust. Flame*, 133:173–188, 2003. doi:10.1016/S0010-2180(02)00574-6.